Chapter 8

Inter-Subject Non-Rigid Registration: An Overview with Classification and the Romeo Algorithm

Pierre Hellier[1]

8.1 Introduction

Registration is basically the process of estimating the spatial transformation that matches two images. Registration is especially important when analyzing motion and deformations of natural phenomena. Registration is a very active field of research. Various techniques have been proposed so far, concerning rigid and non-rigid methods.

Rigid registration is adapted in many applications except in some situations: complex deformations such as soft tissue deformation, evolution of lesions over time, matter appearance or dissipation and so on. Therefore, non-rigid registration methods (also called deformable registration) have been developed. This chapter will be mostly concerned with non-rigid registration methods and more particularly with a specific application: registration of brains of different subjects.

During the last few years, the development of electronic brain atlases has emerged by overcoming some limitations of traditional paper-based atlases [49, 62, 81, 92, 97, 139]. To do so, non-rigid intersubject registration methods have been developed in order to account for the intersubject variability [92].

[1]IRISA-INRIA, Campus de Beaulieu, 35042 Rennes, France

Electronic atlases have two main purposes:

- Automatic segmentation of a given subject by matching the segmentation and labeling of anatomical structures of a template. Labels of the template can be deformed into another subject, under the assumption that there is a total relation between the points of the atlas (source) and the points of the studied subject (target). This objective has been pursued for a long time in medicine and was traditionally treated by paper atlases with generally rather simple transformations. The most known example is the atlas of Talairach with its famous AC-PC referential and its related proportional squaring [131].

- Understanding of brain functions. Many techniques have been developed to record brain activity (SPECT, PET, MEG/EEG, fMRI). However, the links between anatomy and functional organization are often not well known: the superimposition of multiindividual neurofunctional recordings on the same anatomy is useful to better understand the human brain functional organization. In this case, inherent anatomical variability between individuals may disturb this interpretation. Therefore, spatial normalization, which is the goal of non-rigid registration methods, makes it possible to study the functional variability. A better knowledge of this anatomy-function relationship is of great interest for the researcher in cognitive neuroscience, as well as for the surgeon and the neurologist who intend to delineate relevant functional areas before surgery.

This chapter is divided into two sections: an overview with classification of non-rigid registration techniques will be presented first. The Romeo algorithm (robust multigrid elastic registration based on optical flow) will then be described.

8.2 Overview of Non-Rigid Registration Methods

8.2.1 Introduction

Non-rigid registration is a very active field of research and numerous methods have been proposed. This section does not intend to propose an exhaustive

list of methods but to present generic and up-to-date methods. The interested reader will refer to [19, 60, 61, 87, 90, 91, 140, 143, 151] for a complete survey on this subject. This section will therefore be restricted to an overview with classification of non-rigid registration methods, more particularly applied to non-rigid registration of brains of different subjects.

Methods can generally be classified according to the following criteria:

- Features that will be matched. This includes both the dimension of the data (classically from $2D$ to $4D$) as well as the homologous structures that are chosen for matching.
- Transformation type. This includes the transformation domain: local or global. A transformation is called "global" when the modification of one parameter affects the entire image. This also includes the transformation type (rigid, affine, projective and so on).
- The similarity measure. The similarity models the interaction between the data (features used for matching defined above) and the variables to be estimated (parameters of the transformation for instance).
- The regularization. The regularization can be implicit (regularized transformation model for instance) or explicit (first-order regularization for instance).
- The optimization method. Once the registration problem has been formalized, the optimization plays a crucial role in estimating the registration variables.

We have chosen to divide non-rigid registration methods into two classes: geometrical methods that are based on the extraction and matching of sparse features; and photometric (or intensity-based) methods that exploit luminance information directly.

8.2.2 Geometric Methods

The amount of data in a 3D MR image is enormous: it contains more than 10 million voxels. The computation of a dense deformation field is a tough problem: more than 40.10^6 variables have to be estimated. This complexity has motivated geometric methods: sparse anatomical features reduce the dimension of the

problem. Methods that are presented here extract geometrical features from images and compute a transformation that matches these features while interpolating smoothly the deformation throughout the image.

8.2.2.1 Points

Earliest methods rely on points. The most famous one, which is still a reference in the field of neuroscience, is the Talairach stereotaxic space [130]. It has then been extended to the Talairach proportional squaring system [132]. Both methods rely on the identification of the anterior comissure AC and posterior comissure PC, as well as five brain extrema which makes it possible to specify a partition of the volume into 12 subvolumes. The transformation associated with the Talairach proportional squaring system is a piecewise linear one that makes it possible to embed the brain into a "box" centered at AC and whose anatomical axes are known. This framework is known to be quite accurate in the central region but less accurate for cortical areas.

Other authors have proposed methods based on anatomical points to register brains of different subjects [16, 26, 50, 116]. However, the number of points that can be reproducibly identified among a population of subjects is limited. It has been evaluated as 36 [38] or 26 [50]. This number of points seems limited to understand the intersubject variability; in addition to this, the extraction step might be erroneous. To limit the dependency toward extraction, some authors have proposed differential geometry operators to automate the process [135, 114, 115].

8.2.2.2 Curves

Guéziec [66], Subsol [126] and Declerck [41] describe methods to register two volumes thanks to curves: smoothing and curve matching in [66], application to the registration of brains in [41], building of skull atlases in [126]. Crest lines, introduced by Monga *et al.* [100], are defined as maximal curvature points and can be automatically extracted using the marching lines algorithm [137].

Gueziec *et al.* [66] approximate curves using B-splines. This enables the direct computation of features such as position, curvature and so on. Curves are then registered using an iterative approach like the Kalman filter. Subsol [126] and Declerck [41] have extended the ICP algorithm (Iterative closest points

proposed by Zhang [150] and Besl [12]). The iterative approach matches each point with the closest point on the target curve. [41] models the transformation as a B-spline while [126] estimates successively a rigid, affine, polynomial and spline transformation.

8.2.2.3 Surfaces

In 3D medical imaging, anatomical structures are likely to be closed surfaces than points or curves. Several authors [51, 56, 138, 128] have therefore proposed methods to register brain surfaces (like ventricles, central nuclei, brain surface). In a nutshell, deformable models have been extensively used for segmentation of medical images [8, 15, 94]. They can lead either to an explicit representation of contours (e.g., snakes) or to an implicit representation of contours (e.g., level sets [124]).

Thompson and Toga [138] have proposed an original method based on the extraction and matching of the cortical surface. Surfaces are first modeled by a superquadric [25] than refined by the "balloons" method [32]. Feldmar *et al.* [52] have extended the curve matching methods (see Section 8.2.2 to the registration of free-form surfaces. The iterative approach matches points of similar curvature.

8.2.2.4 From "Contour" to Volume

We have previously presented registration methods based on the extraction and matching of sparse features. The next step is to extrapolate smoothly the deformation to the entire volume. To do so, two kinds of approaches can be used: thin plate spline methods and free form deformations.

The thin plate spline (TPS) approach consists in minimizing a functional under constraints. Initiated by Duchon [47] and Meinguet [95], this method is now widespread, thanks to the work of Bookstein [16]. The problem can be formulated as the minimization of:

$$\min_u \int |\nabla^m u(x)| dx, \text{ under the constraint } \forall i \in E, u(a_i) = \alpha_i,$$

where u is the deformation field, E is the set of contour points, a_i being matched with α_i. Bookstein describes the TPS method that minimizes the energy of a thin plate under constraint. The solution can be expressed as local

solutions of the biharmonic equation $\triangle^2 U = 0$ at different scales. Solutions are expressed as $z(x, y) = -U(r) = -r^2 \log(r^2)$ in dimension 2 (with $r = \sqrt{x^2 + y^2}$) and $z(x, y) = |r|$ in dimension 3 (with $r = \sqrt{x^2 + y^2 + z^2}$). This spline transformation ensures the matching of landmarks as well as a smooth interpolation of the deformation. Chui and Rangarajan have proposed the TPS-RPM algorithm [30] where they address both the correspondence and the transformation problem. They propose the softassign algorithm to solve the correspondence problem and the TPS for the transformation.

Another approach is the use of free-form deformations [123]. Initially introduced to model and deform objects [6, 148], they have also been used to model deformations [43, 64, 70, 96, 107, 117, 129, 134]. Splines models are quite powerful to extrapolate deformations indeed.

8.2.3 Photometric Methods

The number of features that can be extracted reproductively among a population of subjects is rather low. Therefore, photometric (also called "intensity-based" or iconic) methods have been developed to take into account the entire information of the volume. Photometric methods rely on a similarity (or dissimilarity) that measures the dependency between two volumes. We have chosen to present the registration methods according to the following classification: methods that derive from the laws of continuum mechanics; methods that use cross-correlation; the demon's method; methods based on optical flow, and finally methods that estimate jointly an intensity correction and a geometrical transformation.

8.2.3.1 Models Based on Continuum Mechanics

Considering two MR images of two different subjects, the estimation of a "plausible" transformation must be sought. The notion of a "plausible" transformation in this context being particularly difficult to state, some authors have proposed to comply with the laws of continuum mechanics, either elastic or fluid (Section 8.2.3).

8.2.3.2 Elastic Models

Elastic models have been introduced by Broit [18] and extended by Bajcsy and Kovacic [4, 5]. These models are nowadays used by various authors [39, 38, 54,

59, 104, 105, 118, 121, 146]. The estimated deformation field should basically obey the rule of the Navier equation:

$$\mu\nabla^2 u + (\lambda + \mu)\nabla(div(u)) + F = 0,$$

where u is the deformation field to estimate, λ and μ are the Lame coefficients and F is the sum of forces that are applied on the system. The problem is to specify the forces F that will lead to a correct registration. Bajcsy proposes to compute these forces so as to match the contours [5]. Davatzikos [39] and Peckar [104] do not compute any forces but segment the brain surface and the ventricles using two different methods. The matching of these surfaces provide boundary conditions that make it possible to solve the problem. These two approaches are therefore sensitive to segmentation errors.

The use of elastic methods raises the following questions:

- What should be the values of Lame coefficients? The choice of these coefficients influence the deformation. Earliest work proposed that $\lambda = 0$ but it appears nowadays to be a limitation.
- This modeling cannot handle large deformations. As a matter of fact, the equation of Navier is only valid for small displacements. To solve this problem, two kind of approaches can be used. A rigid registration can provide a good initialization (Bajcsy [5] uses principal inertia axes and Davatzikos [38] uses the stereotaxic space). Another way [104] is to solve the problem iteratively using a multiresolution approach.
- The topology of present structures will be preserved. This may be interesting in some applications but more questionable when matching brains of different subjects. Ono [103] has shown that cortical structures are not topologically equivalent among subjects indeed.

8.2.3.3 Fluid Models

Following the same inspiration as elastic models, Christensen and Miller [27] propose to compute a deformation that obeys the rule of fluid mechanics (equation of Navier–Stokes). The major difference with the elastic modeling is the fact that the fluid continuously "forgets" about its initial position. Large displacements and complex motions are therefore much easier to handle. The equation

of Navier–Stokes can be written as

$$\frac{\partial \vec{u}}{\partial t} - \nu \triangle \vec{u} + (\vec{u} \cdot \vec{\nabla})\, \vec{u} + \vec{\nabla} p = 0$$

where ν is the fluid viscosity, $\vec{u}$ its speed and $\vec{p}$ its pressure. This equation is highly non-linear (cross-terms) and its resolution is complex, leading to large computation times. Christensen imposes the constraint that the Jacobian be positive [27], leading to an homeomorphic transformation.

Christensen and Johnson [28] have extended the registration approach to introduce the reversibility constraint. Given two subjects A and B, the method jointly estimates transformation from A to B and from B to A. The inverse consistency error is zero when the forward and reverse transformations are inverses of one another. Furthermore, the transformations obey the rules of continuum mechanics and are parameterized by Fourier series.

Bro-Nielsen [17] has proposed an improvement to solve the following partial differential equation:

$$\mathcal{L}v = \mu \nabla v(x) + (\lambda + \mu)\, div(v) = f(x, u\,(x))$$

where u is the displacement and v the instantaneous speed. For a small time change, internal forces are constant and the equation is linear. While Christensen uses a finite element scheme, Bro-Nielsen considers the impulse response associated with operator $\mathcal{L}$. The solution is then expressed as linear combinations of eigenvectors of operator $\mathcal{L}$. This significantly decreases the computation time.

Wang and Staib [146] have also proposed two methods that obey the rule of continuum mechanics. The methods respect the properties of elastic solids or viscous fluids. A statistical shape information (sparse set of forces) is mixed with a luminance information (dense set of forces within a Bayesian framework).

8.2.3.4 Correlation

Cross-correlation is a widespread similarity measure. It has been used by popular methods such as ANIMAL [35] and Gee *et al.* [59]. ANIMAL uses a multiresolution strategy to estimate local linear transformations that maximizes cross-correlation. At a resolution level σ, the regularization is based on the statement that the norm of displacement vectors should not exceed σ. Colllins *et al.* [36] has extended ANIMAL so that sulcal constraints can be taken into account in the registration process.

Gee, first interested in mechanical models [59], adopted a statistical Bayesian framework [58]. Let us note I_R the reference volume, I_T the target volume, $z = \{I_R, I_T\}$ the data and u the deformation field. The problem is then to minimize the cost functional:

$$P(z|u) \propto \exp -\{\int_{x \in \Omega_T} S\left(I_T(x), I_R(x + u\left(x\right))\right) dx\},$$

where S is the similarity measure that has been chosen to be cross-correlation. The regularization follows either a membrane model $P(u) \propto \lambda \int (u_x^2 + u_y^2)\, dx$ or a thin-plate model $P(u) \propto \lambda \int (u_{xx}^2 + 2u_{xy}^2 + u_{yy}^2)\, dx$. Gee also made it possible to incorporate landmark points in the registration process. If the transformation X matches p_i with p_i', the associated potential is: $P(Z = (p_i, p_i')|\theta = X) \propto \exp -\frac{1}{2\sigma_i^2} ||X\left(p_i\right) - p_i'||^2$. This probabilistic approach is useful to mix mechanical regularization, photometric similarity and landmark matching. It also make it possible to experiment and compare different kinds of regularization [58].

Cachier *et al.* [21] have proposed the Pasha algorithm where the local correlation coefficient is used. This coefficient can be efficiently computed using convolutions with a Gaussian window function. The regularization is a mixture of competitive and incremental regularization using quadratic energies.

8.2.3.5 Demons

Thirion has proposed a method well known as the Demon's algorithm [136]. At each demon's location, force is computed so as to repulse the model toward the data. The force depends on the polarity of the point (inside or outside the model), the image difference and gradients. For small displacements, it has been shown that the demon's method and optical flow are equivalent. The method is alternated: computation of forces and regularization of the deformation field by a Gaussian smoothing. The choice of the smoothing parameter is therefore important. The Demon's algorithm has been successfully used by Dawant *et al.* [40].

Cachier and Pennec [106] have shown that the Demon's method can be viewed as a second-order gradient descent of the SSD (Sum of Square Differences). This amounts to a minmax problem: maximization of similarity and regularization of solution.

8.2.3.6 Displaced Frame Difference and Optical Flow

The displaced frame difference (DFD) measures the difference between voxel intensities. It can be used either directly [1, 101, 144] or linearized (known as optical flow) [46, 76, 125]. The DFD is known to be highly non-linear whereas optical flow is linear. However, optical flow is only valid for small displacements and can estimate motion only in the direction of the image gradient (aperture problem). In both cases, this similarity will not be valid if luminance is not conserved (this may happen because of image acquisition, acquisition systems or parameters, MR inhomogeneities and so on).

Close to mechanical approaches, Song and Leahy [125] and Devlaminck [46] have proposed to estimate the optical flow with a mechanical regularization. More specifically, when images are density images (the luminance is directly related to a physical quantity), the mass conservation hypothesis may be introduced to constraint the estimation in a plausible way [37, 125].

In the field of cardiac imaging, Reissmann *et al.* [112] have proposed to use the neuractive pyramid to register images using the optical flow. The elastic grid that is the kernel of the deformation deforms so as to reject the discontinuities at boundaries of the grid. The minimization is therefore alternated between the deformation and the optimal shape of the grid.

The SPM spatial normalization approach [2] estimates warps by matching each skull-stripped image to the skull-stripped reference. Registration involves minimizing the mean squared difference between the images, which had been previously smoothed by convolving with an isotropic 8 mm FWHM Gaussian kernel. The non-rigid deformation is modeled by a linear combination of low-frequency cosine transform basis functions [2]. Displacements in each direction are parameterized by 392 basis function coefficients, making a total of 1176 parameters in total. Regularization is obtained by minimizing the membrane energy of the warps.

Vemuri [144] also uses the optical flow but models the deformation as a combination of splines similarly to [127]. Finally, Musse *et al.* [101] describe a hierarchical method to estimate the deformation using the SSD criterion. The solution is sought as a combination of the spine's functions that ensure the regularity of the solution.

8.2.3.7 Joint estimation of Intensity and Geometric Transformations

Many artifacts can modify the luminance of an MR image. One of them is the inhomogeneity of the magnetic field for instance [80]. As a consequence, the hypothesis of luminance conservation might not be valid anywhere. One solution consists in using robust estimators to get rid of inconsistent data. Another solution consists in estimating jointly an intensity correction and a spatial transformation [53, 55, 65].

Gupta and Prince [65] propose an affine correction model for tagged MR: $f(\mathbf{r}+\mathbf{dr}, t+dt) = m(\mathbf{r}, \mathbf{dr}, t, dt)\, f(\mathbf{r}, t) + c(\mathbf{r}, \mathbf{dr}, t, dt)$. The optical flow equation then becomes:

$$f(\mathbf{r}, t) + \nabla f\,(\mathbf{r}, t) \cdot U(\mathbf{r}, t) - f(\mathbf{r}, t)\frac{\partial m\,(\mathbf{r}, t)}{\partial t} - \frac{\partial c(\mathbf{r}, t)}{\partial t} = 0.$$

The equation is solved in a variational framework using a first-order regularization.

Friston [55] and Feldmar [53] propose to embed the intensity correction and the spatial transformation in the same cost functional:

$$\mathcal{C}(\mathbf{f}, g) = \sum_{M_i \in i_1} (I_2(f(M_i)) - g(I_1(M_i), M_i))^2,$$

where f is the 3D transformation and g is the intensity correction. Feldmar generalizes this approach and considers 3D images as 4D surfaces. The criterion becomes:

$$\mathcal{C}(\mathbf{f}, g) = \sum_{(x_j, i_j)} d\,((\mathbf{f}\,(x_j), g(x_j, i_j)), CP_{4D}(\mathbf{f}(x_j), g(x_j, i_j)))^2,$$

where x_j is the point of intensity i_j and CP_{4D} is the function that renders the closest point. In this sense, this method is a generalization of the ICP (iterative closest point) algorithm. Functions f and g can be modeled according to the application. For instance, for a intra-subject monomodal registration, f is rigid and g is the identity. For inter-subject registration, f can be a combination of radial basis functions and f should correct acquisition artifacts.

8.2.3.8 Non-Rigid Multimodal Registration

Although many efforts have been made to perform rigid multimodal registration, as far as we know, there has been few research concerning non-rigid multimodal registration. As a matter of fact, this is quite a challenging problem, since the number of variables to be estimated can be very large (intensity mapping, and geometrical transformation, the two being dependent). Two different approaches have been developed.

One option is to estimate the geometrical transformation with the original intensities of the two images to be registered. In this category, Maintz *et al.* [89] and Gaens *et al.* [57] proposed an algorithm that seek a non-rigid transformation by maximization of mutual information. They use a "block-matching" minimization scheme with a Gaussian filtering of the estimated deformation field to avoid blocky effects. On local windows, the estimation does not take into account the spatial context of the deformation field and only a translation is estimated. Furthermore, these methods are only performed in 2D. Rueckert *et al.* [117] and Kybic *et al.* [84] proposed an approach based on cubic B-splines and mutual information. The spline deformation model intrinsically contains the regularization and provides a smooth interpolation of the field. Displacement of the nodes are computed such as to maximize the similarity measure (mutual information, or normalized mutual information).

Another appealing option has been proposed by Guimond *et al.* [63]. This method considers the multimodal registration problem as a monomodal registration problem, and therefore estimates alternatively an intensity correction and a monomodal registration. The originality of the method resides in the decomposition of the problem into two "easier" ones: a polynomial intensity mapping and a monomodal registration problem based on the demon's algorithm [136].

8.2.4 Discussion

This section has presented a brief overview of non-rigid registration techniques. Methods have been arbitrarily classified into two groups: geometric methods that rely on the extraction and matching of geometrical features; and photometric methods (or intensity-based) that rely on the luminance information directly.

Geometric methods are attractive because they rely on anatomical features. The deformation is expected to be consistent in the vicinity of features that are used. In addition, the complexity is significantly reduced compared to the

method that uses the entire data. Despite these advantages, these methods appear limited in the context of inter-subject registration. As a matter of fact, the number of features that can be reproductively identified among a population of subjects is limited compared to the inter-subject variability. Furthermore, a lot of information present in the data are not used by geometric methods while photometric take advantage of all information available. This rapid comparison may explain the popularity of photometric methods, which has been proved in the particular context of rigid multimodal fusion [147].

Photometric methods differ by numerous aspects. Among them, two important ones are the similarity measure and the regularization.

The choice of the similarity is crucial since this models the interaction between the data and the estimated variables. Roche *et al.* have shown [113] that the choice of a similarity can be guided by the a priori knowledge that we have about the data. Regularization is also crucial since it expresses the a priori knowledge that we have about the deformation. The choice of a correct regularization in the context of inter-subject normalization is difficult and still debated since we do not know what should be the "ideal" deformation field between two brains of two different subjects. Regularization often conserves the topology of brain structures. While valid for internal structures such as ventricles, the conservation of topology is a strong hypothesis when dealing with cortical structures. Anatomists have indeed shown that cortical sulci have different shapes and topology among individuals [103].

Recently there has been an increasing number of promising methods [22, 29, 36, 68, 73, 79, 141] that combine the benefits of photometric and geometric approaches to register brains of different subjects. In these methods, landmarks are used to drive the registration process so that the deformation field is consistent with the matching of sparse anatomical structures.

8.3 Romeo: Robust Multigrid Elastic Registration Based on Optical Flow

8.3.1 Introduction

We consider the registration problem as a motion estimation problem, which has been studied by different authors [7, 9, 10, 11, 13, 31, 76, 82, 102, 120]. Our

3D method performs a non-linear multimodality registration of MRI acquisition of different subjects. The similarity measure that we use incorporates robust estimators whose utility is twofold: on the one hand we want to limit the influence of the acquisition noise, on the other hand, we want to cope with possible modifications of structures' topology [75].

Since the luminance of MR images might not be directly comparable, we propose an intensity correction scheme that is anatomically consistent [71]. This correction method will be described in Section 8.3.2. Then volumes to be registered are rigidly aligned by maximizing mutual information (described in Section 8.3.2).

Many tasks in computer vision may be expressed as the minimization of a cost function. The optimization is often difficult to achieve, because the cost function is non-convex and because the optimization involves a very large number of variables. Therefore efficient iterative multigrid (or multilevel) approaches have been developed [67, 93] and applied in motion estimation [48] and in early vision [133].

To take into account large deformations, we use a multiresolution optimization scheme. Besides, at each resolution level, we use a multigrid minimization to accelerate the algorithm and improve the quality of the estimation. Within this hierarchical approach, we designed an adaptive partition of the volume to refine the estimation on the regions of interest and avoid useless efforts elsewhere. An anatomical segmentation of the cortex is introduced and used in two ways: at each resolution level, we initialize the partition as an octree subdivision based on the segmentation, and the segmentation mask is used in the subdivision criterion which controls the refinement of the estimation.

The method will first be extensively presented in Section 8.3.2. We will also present an extension of this method to multimodal data [72] in Section 8.3.2. Results on synthetic and real data will then be presented in Section 8.3.3.

8.3.2 Method

8.3.2.1 General Formulation

The optical flow hypothesis, or brightness constancy constraint, introduced by Horn and Schunck [76], assumes that the luminance of a physical point does not vary much between the two volumes to register. It amounts to zeroing the

so-called DFD (displaced frame difference):

$$f(s + \boldsymbol{w}_s, t_1) - f(s, t_2) = 0,$$

where s is a voxel of the volume, t_1 and t_2 are the indexes of the volumes (temporal indexes for a dynamic acquisition, indexes in a database for multisubject registration), f is the luminance function and $\boldsymbol{w}$ the expected 3D displacement field. The DFD may not be valid everywhere, because of noise and intensity inhomogeneities of MR acquisition. The robustness of the registration process with respect to acquisition artifacts will be discussed later on, the sections 8.3.2 and 8.3.3.

Generally, a linear expansion of this equation is preferred : $\boldsymbol{\nabla} f(s,t) \cdot \boldsymbol{w}_s + f_t(s,t) = 0$ where $\boldsymbol{\nabla} f(s,t)$ stands for the spatial gradient of luminance and $f_t(s,t)$ is the voxelwise difference between the two volumes. The resulting set of undetermined equations has to be complemented with some prior on the deformation field. Using an energy-based framework (which can be viewed either from the Bayesian point of view, or from the one of the regularization theory), the registration problem may be formulated as the minimization of the following cost function:

$$U(\boldsymbol{w}; f) = \sum_{s \in S} [\boldsymbol{\nabla} f(s,t) \cdot \boldsymbol{w}_s + f_t(s,t)]^2 + \alpha \sum_{<s,r> \in \mathcal{C}} ||\boldsymbol{w}_s - \boldsymbol{w}_r||^2, \tag{8.1}$$

where S is the voxel lattice, $\mathcal{C}$ is the set of neighboring pairs w.r.t. a given neighborhood system $\mathcal{V}$ on S ($<s,r> \in \mathcal{C} \Leftrightarrow s \in \mathcal{V}(r)$), and α controls the balance between the two energy terms. The first term captures the brightness constancy constraint, thus modeling the interaction between the field (unknown variables) and the data (given variables), whereas the second term captures a simple smoothness prior. The weaknesses of this formulation are known:

(a) Due to the linearization, the optical flow constraint (OFC) is not valid in case of large displacements.

(b) The OFC might not be valid in all the regions of the volume, because of the acquisition noise, intensity non-uniformity in MRI data, and occlusions.

(c) The "real" field is not globally smooth and it probably contains discontinuities that might not be preserved because of the quadratic smoothing.

To cope with the (b) and (c) limitations, we replace the quadratic cost by robust functions. To face the problem (a), we use a multiresolution plan and a multigrid strategy to improve the minimization at each resolution level.

We have here introduced a simple regularization term that makes almost no assumption on the estimated deformation field. One could imagine choosing different regularizations for the different brain tissues, but that involves specific assumptions on the "real" deformation that we do not address in that paper. However, the introduction of a robust estimator on the regularization term makes it possible to take into account possible discontinuities on the border of structures having different physical properties.

8.3.2.2 Rigid Registration Step

Given two images with potentially large displacement, it first seems reasonable to estimate a rigid transformation. This step is performed by estimating a rigid transformation that maximizes mutual information [33, 145]. Given two images A and B, considered as discrete random variables, let us note $p_A(a)$ and $p_B(b)$ their respective marginal probability distribution, and $p_{A,B}(a, b)$ the joint distribution. Mutual information $I(A, B)$ is then defined as [33, 145]:

$$I(A, B) = \sum_{a,b} p_{A,B}(a, b) \log_2 \frac{p_{A,B}(a, b)}{p_A(a) p_B(b)} = H(A) + H(B) - H(A, B),$$

with

$$H(A) = -\sum_{a} p_A(a) \log_2(p_A(a)) \quad \text{and}$$

$$H(A, B) = -\sum_{a,b} p_{A,B}(a, b) \log_2(p_{A,B}(a, b)).$$

In some particular cases, such as brain images for instance, it is possible to define a reference coordinate system that takes into account some information about the scene (such as resolution of pixels/voxels, orientation of axes, etc.). In such cases, the two volumes to be registered are mapped in this reference coordinate system and the rigid transformation is expressed in this coordinate system. If this a priori information is not available, the rigid transformation is estimated in the coordinate system attached to the data.

The registration is performed through a multiresolution optimization scheme (construction of a pyramid of volumes by successive isotropic Gaussian filtering

and subsampling in each direction) [69, 109]. At each resolution level, the similarity $I(A, T(B))$ is maximized w.r.t. the parameters of the transformation using a Powell's algorithm [110]. We calculate the joint histogram on the overlapping part of A with $T(B)$ by partial volume interpolation, the latter being known to provide a smoother cost function.

8.3.2.3 Intensity Correction

The hypothesis of luminance conservation is strong and cannot stand when considering a large database. Actually, studies nowadays involve distributed databases. Since the MR acquisition can come from different systems, the intensity difference of MR images of different subjects needs to be corrected prior to registration. Let us formulate the problem as:

Given two 3D images I_1 and I_2, and their histograms h_1 and h_2, the problem is to estimate a correction function g such that corresponding anatomical tissues of $g(I_1)$ and I_2 have the same intensity, without registering volumes I_1 and I_2 .

Estimation of Mixture Model. The intensity correction f should be anatomically consistent, i.e., the intensity of gray matter (resp. white matter) of $g(I_1)$ should match the intensity of gray matter (resp. white matter) of I_2. To ensure this coherence, we estimate a mixture of n Gaussian distributions [3, 83, 86, 122, 149] that models the two histograms h_1 and h_2 using the expectation-maximization (EM) algorithm [44] or a stochastic version, the stochastic expectation maximization (SEM) algorithm [23].

Basically, the EM algorithm consists of two steps: Step E where conditional probabilities are computed, and step M where mixtures parameters are estimated so as to maximize the likelihood. Contrary to the EM algorithm, the SEM algorithm consists in adding a stochastic "perturbation" between the E and M step. The labels are then randomly chosen from their current conditional distribution. The SEM algorithm is supposed to be less sensitive to initialization but also to converge more slowly than the EM algorithm.

It is well known that the MR histogram can be roughly modeled as the mixture of five Gaussian laws modeling the main tissues: background, cerebrospinal fluid (CSF), gray matter (GM), white matter (WM) and a mixture of fat and muscle. The Gaussian mixture has proved to be relevant for fitting MR-T1 histograms [83]. It has also been shown that mixture tissues (interface gray-CSF and

Gray-White) can also be modeled by additional Gaussian laws to model partial-volume effects. To do so, a mixture of seven models can be used instead.

In every case (EM or SEM algorithm, five or seven Gaussian models), we model each class κ by a Gaussian distribution of mean μ_κ (respectively, ν_κ) for image I_1 (respectively, image I_2).

Parametric Correction. To align the intensities of the anatomical tissues and to interpolate smoothly the correction, we choose a polynomial correction function of order p (see [63] for a similar modeling of intensity correction) such that $g^p(x) = \sum_{i=0}^{i=p} \theta^i x^i$. The coefficients θ^i are estimated such as to minimize the following cost:

$$\sum_{l=1}^{l=n} \left(g^p(\mu_j) - \nu_j\right)^2 .$$

The intensity correction aims at aligning the mean values of each classes while interpolating smoothly between the samples. This least-square problem amounts to inverting a linear system of order p. The resulting correction can then be applied to the voxel intensities of volume I_1.

8.3.2.4 Robust Estimators

Cost function Eq. (8.1) does not make any difference between relevant data and inconsistent data, nor between neighboring pairs where the field is smooth and neighboring pairs where the field is discontinuous. Therefore, we introduce robust functions [77] and more precisely two robust M-estimators [14], the first one on the data term and the second one on the regularization term. We do not describe in details the properties of robust M-estimators, referring the reader to [14, 98] for further explanations. The cost function (8.1) can then be modified as:

$$U(\boldsymbol{w}; f) = \sum_{s \in S} \rho_1 \left(\nabla f(s,t) \cdot \boldsymbol{w}_s + f_t(s,t)\right) + \alpha \sum_{<s,r> \in \mathcal{C}} \rho_2 \left(||\boldsymbol{w}_s - \boldsymbol{w}_r||\right). \quad (8.2)$$

According to some properties of robust M-estimators [14, 24], it can be shown that the minimization of U (Eq. 8.1) is equivalent to the minimization of an augmented function, noted $\overset{*}{U}$:

$$\begin{aligned} \overset{*}{U}(\boldsymbol{w}, \delta, \beta; f) = & \sum_{s \in S} \delta_s \left(\nabla f(s,t) \cdot \boldsymbol{w}_s + f_t(s,t)\right)^2 + \psi_1(\delta_s) + \alpha \\ & \times \sum_{<s,r> \in \mathcal{C}} \beta_{sr} ||\boldsymbol{w}_s - \boldsymbol{w}_r||^2 + \psi_2(\beta_{sr}), \end{aligned} \quad (8.3)$$

where δ_s and β_{sr} are auxiliary variables (acting as "weights") to be estimated. This cost function has the advantage to be quadratic with respect to $\boldsymbol{w}$. It also shows clearly that, when a discontinuity gets larger, the contribution of the pair of neighbors is limited by the reduction of the associated weight β_{sr}. The minimizers of $\overset{*}{U}$ with respect to the auxiliary variables are obtained in closed form [14, 24]. The overall minimization of such function consists in an alternated weights computation and quadratic minimizations (with respect to $\boldsymbol{w}$).

8.3.2.5 Multiresolution Incremental Computation of the Optical Flow

In cases of large displacements, we use a classical incremental multiresolution procedure [11, 48] (see Fig. 8.1). We construct a pyramid of volumes $\{f^k\}$ with successive Gaussian smoothing and subsampling in each direction [20]. For each direction $i = x, y, z$, d_i is the spatial resolution of a voxel (the spatial resolution of MR acquisition is around 1 mm, depending on the system). We perform a Gaussian filtering using the recursive implementation proposed in [45] with a standard deviation of $2d_i$ in direction i, in order to satisfy Nyquist's criterion. This implementation allows to perform infinite impulse response filtering at a constant computation cost.

At the coarsest level, displacements are reduced, and cost function (8.3) can be used because the linearization hypothesis becomes valid. For the next resolution levels, only an increment $\mathrm{d}\boldsymbol{w}^k$ is estimated to refine the estimate $\hat{\boldsymbol{w}}^k$ obtained

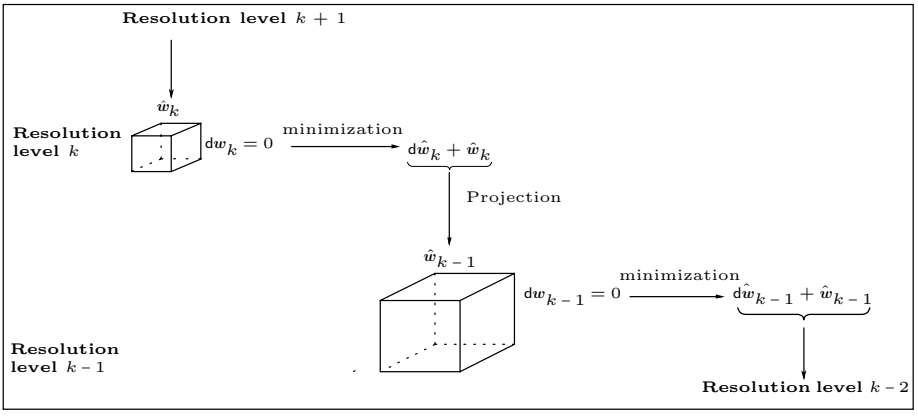

Figure 8.1: Incremental estimation of the optical flow.

from the previous level. We perform the registration from resolution k_c until resolution k_f (in general $k_f = 0$). This is done using cost function (8.2) but with $\nabla \tilde{f}^k(s,t) \triangleq \nabla f^k(s + \hat{\boldsymbol{w}}_s^k, t_2)$ and $\tilde{f}_t^k(s,t) \triangleq f^k(s + \hat{\boldsymbol{w}}_s^k, t_2) - f^k(s, t_1)$ instead of $\nabla f^k(s,t)$ and $f_t^k(s,t)$.

To compute the spatial and temporal gradients, we construct the warped volume $f^k(s + \hat{\boldsymbol{w}}_s^k, t_2)$ from volume $f^k(s, t_2)$ and the deformation field $\hat{\boldsymbol{w}}_s^k$, using trilinear interpolation. The spatial gradient is hence calculated using the recursive implementation of the derivatives of the Gaussian [45]. At each voxel, we calculate the difference between the source volume and the reconstructed volume, and the result is filtered with a Gaussian to construct the temporal gradient. As previously, these quantities come from the linearization of the constancy assumption expressed for the whole displacement $\hat{\boldsymbol{w}}_s^k + \mathrm{d}\boldsymbol{w}_s^k$. The regularization term becomes $\sum_{<s,r>\in\mathcal{C}} \rho_2(||\hat{\boldsymbol{w}}_s^k + \mathrm{d}\boldsymbol{w}_s^k - \hat{\boldsymbol{w}}_r^k - \mathrm{d}\boldsymbol{w}_r^k||)$.

8.3.2.6 Multigrid Minimization Scheme

Motivations. The direct minimization of Eq. (8.3) is intractable. Some iterative procedure has to be designed. Unfortunately, the propagation of information through local interaction is often very slow, leading to an extremely time-consuming algorithm. To overcome this difficulty (which is classical in computer vision when minimizing a cost function involving a large number of variables), multigrid approaches have been designed and used in the field of computer vision [48, 98, 133]. Multigrid minimization consists in performing the estimation through a set of nested subspaces. As the algorithm goes further, the dimension of these subspaces increases, thus leading to a more accurate estimation. In practice, the multigrid minimization usually consists in choosing a set of basis functions and estimating the projection of the "real" solution on the space spanned by these basis functions.

Description. At each level of resolution, we use a multigrid minimization (see Fig. 8.2) based on successive partitions of the initial volume [98]. At each resolution level k, and at each grid level ℓ, corresponding to a partition of cubes, we estimate an incremental deformation field $\mathrm{d}\boldsymbol{w}^{k,\ell}$ that refines the estimate $\hat{\boldsymbol{w}}^k$, obtained from the previous resolution levels. This minimization strategy, where the starting point is provided by the previous result—which we hope to be a rough estimate of the desired solution—improves the quality and the

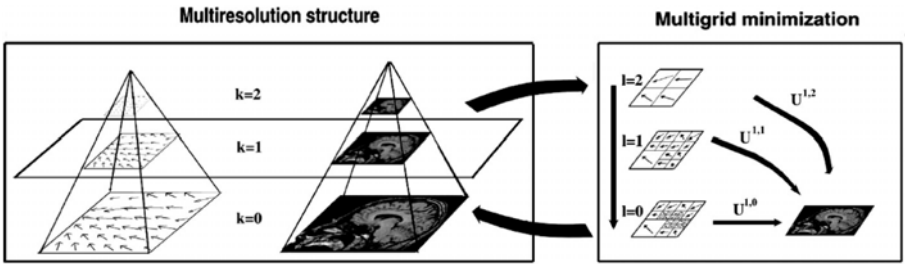

Figure 8.2: Example of multiresolution/multigrid minimization. For each resolution level (on the left), a multigrid strategy (on the right) is performed. For legibility reasons, the figure is a 2D illustration of a 3D algorithm with volumetric data.

convergence rate as compared to the standard iterative solvers (such as Gauss–Seidel).

At grid level ℓ, $\Xi_\ell = \{\Xi_n, n = 1, \ldots, N_\ell\}$ is the partition of the volume B into N_ℓ cubes Ξ_n. At each grid level ℓ corresponds a deformation increment $\mathrm{T}_{k,\ell}$ that is defined as follows: A 12-dimensional parametric increment deformation field is estimated on each cube Ξ_n, hence the total increment deformation field $\mathrm{d}\boldsymbol{w}^{k,\ell}$ is piecewise affine. At the beginning of each grid level, we construct a reconstructed volume with the target volume $f^k(s, t_2)$ and the field estimated previously (see section 8.3.2). We compute the spatial and temporal gradients at the beginning of each grid level and the increment deformation field $\mathrm{d}\boldsymbol{w}^{k,\ell}$ is initialized to zero. The final deformation field is hence the sum of all the increments estimated at each grid level, thus expressing the hierarchical decomposition of the field.

Contrary to block-matching algorithms, we model the interaction between the cubes (see Section 8.3.2) of the partition, so that there is no "block-effects" in the estimation. At each resolution level k, we perform the registration from grid level ℓ_c until grid level ℓ_f. Depending on the application, it may be useless to compute the estimation until the finest grid level, i.e., $\ell_f = 0$. We will evaluate this fact later on (see section 8.3.3).

Adaptive Partition. To initialize the partition at the coarsest grid level ℓ_c, we consider a segmentation of the brain obtained by morphological operators. After a threshold and an erosion of the initial volume, a region growing process is performed from a starting point that is manually chosen. A dilatation

operation allows us to end up with a binary segmentation. At grid level ℓ_c, the partition is initialized by a single cube of the volume size. We iteratively divide each cube as long as it intersects the segmentation mask and as long as its size is superior to $2^{3\ell_c}$. We finally get an octree partition which is anatomically relevant.

When we change from grid level, each cube is adaptively divided. The subdivision criterion depends first on the segmentation mask (we want a maximum precision on the cortex), but it also depends on the local distribution of the variables δ_s (see Eq. (8.3)). More precisely, a cube is divided if it intersects the segmentation mask or if the mean of δ_s on the cube is below a given threshold. As a matter of fact, δ_s indicates the adequation between the data and the estimated deformation field at voxel s. Therefore, this criterion mixes an indicator of the confidence about the estimation with a relevant anatomical information.

8.3.2.7 Parametric Model

We now introduce the deformation model that is used. We chose to consider an affine 12-parameter model on each cube of the partition. That kind of model is quite usual in the field of computer vision but rarely used in medical imaging. If a cube contains less than 12 voxels, we only estimate a rigid 6-parameter model, and for cubes that contain less than 6 voxels, we estimate a translational displacement field. As we have an adaptive partition, all the cubes of a given grid level might not have the same size. Therefore, we may have different parametric models, adapted to the partition.

At a given resolution level k and grid level ℓ, $\Xi_{k,\ell} = \{\Xi_n, n = 1 \cdots N_{k,\ell}\}$ is the partition of the volume into $N_{k,\ell}$ cubes Ξ_n. On each cube Ξ_n, we estimate an affine displacement defined by the parametric vector $\Theta_n^{k,\ell}$: $\forall s = (x, y, z) \in \Xi_n$, $\mathrm{d}\boldsymbol{w}_s = P_s \Theta_n^{k,\ell}$, with

$$P_s = \begin{pmatrix} 1 & x & y & z & 0 & 0 & 0 & 0 & 0 & 0 & 0 & 0 \\ 0 & 0 & 0 & 0 & 1 & x & y & z & 0 & 0 & 0 & 0 \\ 0 & 0 & 0 & 0 & 0 & 0 & 0 & 0 & 1 & x & y & z \end{pmatrix}.$$

A neighborhood system $V^{k,\ell}$ on the partition $\Xi_{k,\ell}$ derives naturally from $\mathcal{V}$ (see section 8.3.2):

$\forall n, m \in \{1 \cdots N_{k,\ell}\}, m \in V^{k,\ell}(n) \Leftrightarrow \exists s \in \Xi_n, \exists r \in \Xi_m \backslash r \in \mathcal{V}(s)$. $\mathcal{C}$ being the set of neighboring pairs on S^k, we must now distinguish between two types of such pairs: the pairs inside one cube and the pairs between two cubes:

$\forall n \in \{1 \ldots N_{k,\ell}\}, < s, r > \in \mathcal{C}_n^\ell \Leftrightarrow s \in \Xi_n, r \in \Xi_n$ and $r \in \mathcal{V}(s)$.

$\forall n \in \{1 \ldots N_{k,\ell}\}, \forall m \in V^\ell(n), < s, r > \in \mathcal{C}_{nm}^\ell \Leftrightarrow m \in V^l(n), s \in \Xi_n, r \in \Xi_m$

and $r \in \mathcal{V}(s)$.

For the sake of concision, we will now drop the resolution index k. With these notations, the cost function (8.3) becomes

$$\overset{*}{U}{}^{\ell}(\Theta^\ell, \delta^\ell, \beta^\ell; \boldsymbol{w}, f^\ell) = \sum_{n=1}^{N_\ell} \sum_{s \in \Xi_n} \delta_s^\ell \left[\nabla \tilde{f}_s^T P_s \Theta_n^\ell + \tilde{f}_t(s,t)\right]^2 + \psi_1\left(\delta_s^\ell\right)$$
$$+ \alpha \sum_{n=1}^{N_\ell} \left[\sum_{m \in V^\ell(n)} \sum_{<s,r> \in \mathcal{C}_{nm}^\ell} \beta_{sr}^\ell ||\left(\boldsymbol{w}_s + P_s \Theta_n^\ell\right) - \left(\boldsymbol{w}_r + P_r \Theta_m^\ell\right)||^2 + \psi_2\left(\beta_{sr}^\ell\right) \right]$$
$$+ \alpha \sum_{n=1}^{N_\ell} \left[\sum_{<s,r> \in \mathcal{C}_n^\ell} \beta_{sr}^\ell ||\left(\boldsymbol{w}_s + P_s \Theta_n^\ell\right) - \left(\boldsymbol{w}_r + P_r \Theta_n^\ell\right)||^2 + \psi_2\left(\beta_{sr}^\ell\right) \right]. \quad (8.4)$$

Considering the auxiliary variables of the robust estimators as fixed, one can easily differentiate the cost function (8.4) with respect to any Θ_n^ℓ and get a linear system to be solved. We use a Gauss-Seidel method to solve it for its implementation simplicity. However, any iterative solver could be used (solvers such as conjugate gradient with an adapted preconditioning would also be efficient). In turn, when the deformation field is "frozen", the weights are obtained in a closed form [14, 24]. The minimization may therefore be naturally handled as an alternated minimization (estimation of Θ_n^ℓ and computation of the auxiliary variables). Contrary to other methods (minmax problem like the demon's algorithm for instance), that kind of minimization strategy is guaranteed to converge [24, 42, 99] (i.e., to converge toward a local minimum from any initialization).

Moreover, the multigrid minimization makes the method invariant to intensity inhomogeneities that are piecewise constant. As a matter of fact, if the intensity inhomogeneity is constant on a cube, the restriction of the DFD on that cube is modified by adding a constant. As a consequence, minimizing the cost function 8.3.2 gives the same estimate, whenever the cost at the optimum is zero or a constant (see section 8.3.3 for an illustration on that issue).

8.3.2.8 Multimodal Non-Rigid Registration

We have proposed a multimodal version of Romeo [72] where the optical flow is replaced by a more adapted and general similarity measure: mutual information. Mutual information has been presented in the section dedicated to rigid registration (8.3.2).

Let us note $T_{\boldsymbol{w}}$ as the transformation associated with the deformation field $\boldsymbol{w}$. The total transformation $T_{\boldsymbol{w}} \circ T_0$ maps the floating volume B onto the reference volume A. The field $\boldsymbol{w}$ is defined on S_B, where S_B denotes the lattice of volume B (pixel lattice or voxel lattice). The cost function to be minimized then becomes:

$$U(\boldsymbol{w}; A, B, T_0) = -I(A, (T_{\boldsymbol{w}} \circ T_0)(B)) + \alpha \sum_{<s,r> \in \mathcal{C}_B} ||\boldsymbol{w}_s - \boldsymbol{w}_r||^2,$$

where $\mathcal{C}_B$ is the set of neighboring pairs of volume B (if we note $\mathcal{V}$ a neighborhood system on S_B, we have: $< s, r > \in \mathcal{C}_B \Leftrightarrow s \in \mathcal{V}(r)$).

A multiresolution and multigrid minimization are also used in this context. At grid level ℓ and on each cube Ξ_n, we estimate an affine displacement increment defined by the parametric vector Θ_n^ℓ: $\forall s \in \Xi_n$, $d\boldsymbol{w}_s = P_s \Theta_n^\ell$, with $P_s = \mathbb{I}_2 \otimes [1 x_s y_s]$ for 2D images, and $P_s = \mathbb{I}_3 \otimes [1 x_s y_s z_s]$ for 3D images (operator $\otimes$ denotes the Kronecker product).

To be more explicit, in 3D we have:

$$P_s = \begin{pmatrix} 1 & x_s & y_s & z_s & 0 & 0 & 0 & 0 & 0 & 0 & 0 & 0 \\ 0 & 0 & 0 & 0 & 1 & x_s & y_s & z_s & 0 & 0 & 0 & 0 \\ 0 & 0 & 0 & 0 & 0 & 0 & 0 & 0 & 1 & x_s & y_s & z_s \end{pmatrix}.$$

Let us note $T_{\Theta_n^\ell}$, as the transformation associated with the parametric field Θ_n^ℓ. We have $T_{\boldsymbol{\ell}} = T_{d\boldsymbol{w}^\ell}$ and $T_{\Theta_n^\ell} = T_{d\boldsymbol{w}^\ell|_{\Xi_n}}$, where $T_{d\boldsymbol{w}^\ell|_{\Xi_n}}$ denotes the restriction of $T_{\Theta_n^\ell}$ to the cube Ξ_n.

A neighborhood system V^ℓ on the partition Ξ_ℓ derives naturally from $\mathcal{V}$:

$\forall n, m \in \{1 \cdots N_\ell\}$, $m \in V^\ell(n) \Leftrightarrow \exists s \in \Xi_n, \exists r \in \Xi_m / r \in \mathcal{V}(s)$. $\mathcal{C}$ being the set of neighboring pairs on S^k, we must now distinguish between two types of such pairs: the pairs inside one cube and the pairs between two cubes:

$\forall n \in \{1 \ldots N_\ell\}$, $< s, r > \in \mathcal{C}_n^\ell \Leftrightarrow s \in \Xi_n, r \in \Xi_n$ and $r \in \mathcal{V}(s)$.

$\forall n \in \{1 \ldots N_\ell\}, \forall m \in V^\ell(n)$, $< s, r > \in \mathcal{C}_{nm}^\ell \Leftrightarrow m \in V^l(n), s \in \Xi_n, r \in \Xi_m$

and $r \in \mathcal{V}(s)$.

With these notations, at grid level ℓ, the cost function can be modified as:

$$\overset{*}{U}(\Theta^\ell; A, B, \mathrm{T}_0, \boldsymbol{w}^\ell) = -\sum_{n=1}^{N_\ell} I\big(A, \big(\mathrm{T}_{\Theta_n^\ell} \circ \mathrm{T}_{\boldsymbol{w}^\ell} \circ \mathrm{T}_0\big)\big(B_{|\Xi_n}\big)\big)$$
$$+\alpha \sum_{n=1}^{N_\ell} \left[\sum_{m \in V^\ell(n)} \sum_{<s,r> \in \mathcal{C}_{nm}^\ell} ||\big(\boldsymbol{w}_s^\ell + P_s\Theta_n^\ell\big) - \big(\boldsymbol{w}_r^\ell + P_r\Theta_m^\ell\big)||^2 \right]$$
$$+\alpha \sum_{n=1}^{N_\ell} \left[\sum_{<s,r> \in \mathcal{C}_n^\ell} ||\big(\boldsymbol{w}_s^\ell + P_s\Theta_n^\ell\big) - \big(\boldsymbol{w}_r^\ell + P_r\Theta_n^\ell\big)||^2 \right], \tag{8.5}$$

where $B_{|\Xi_n}$ denotes the restriction of volume B to the cube Ξ_n. The minimization is performed with Gauss-Seidel iterative solver (each cube is iteratively updated while its neighbors are "frozen"). On each cube, Powell's algorithm [110, 111] is used to estimate the parametric affine increment.

8.3.2.9 Implementation

The algorithm has been implemented in $C++$ using a template class for volumetric images.[2] A synopsis of the algorithm is presented in Fig. 8.3.

8.3.3 Results

8.3.3.1 Intensity Correction

We have evaluated the approach on various MR acquisitions. We present results on real data of the intensity correction, comparing the EM and SEM approaches and comparing the number of Gaussian laws used to model the histogram.

We have tested the approach on various T1-MR images and the algorithm has proved to be robust and reliable. Furthermore, it does not require any spatial alignment between the images to be corrected and can therefore be applied in various contexts: MR time series or MR of different subjects. Figure 8.4 presents cut-planes images of volumetric MR.

Figure 8.5 presents the effect of the correction using a EM algorithm and Fig. 8.6 the correction using a SEM algorithm. For each estimation scheme, we test a mixture of five (left) and seven Gaussian distributions to model the histogram. In each case, a fourth order parametric correction has been estimated.

[2] http://www.irisa.fr/vista/Themes/Logiciel/VIsTAL/VIsTAL.html

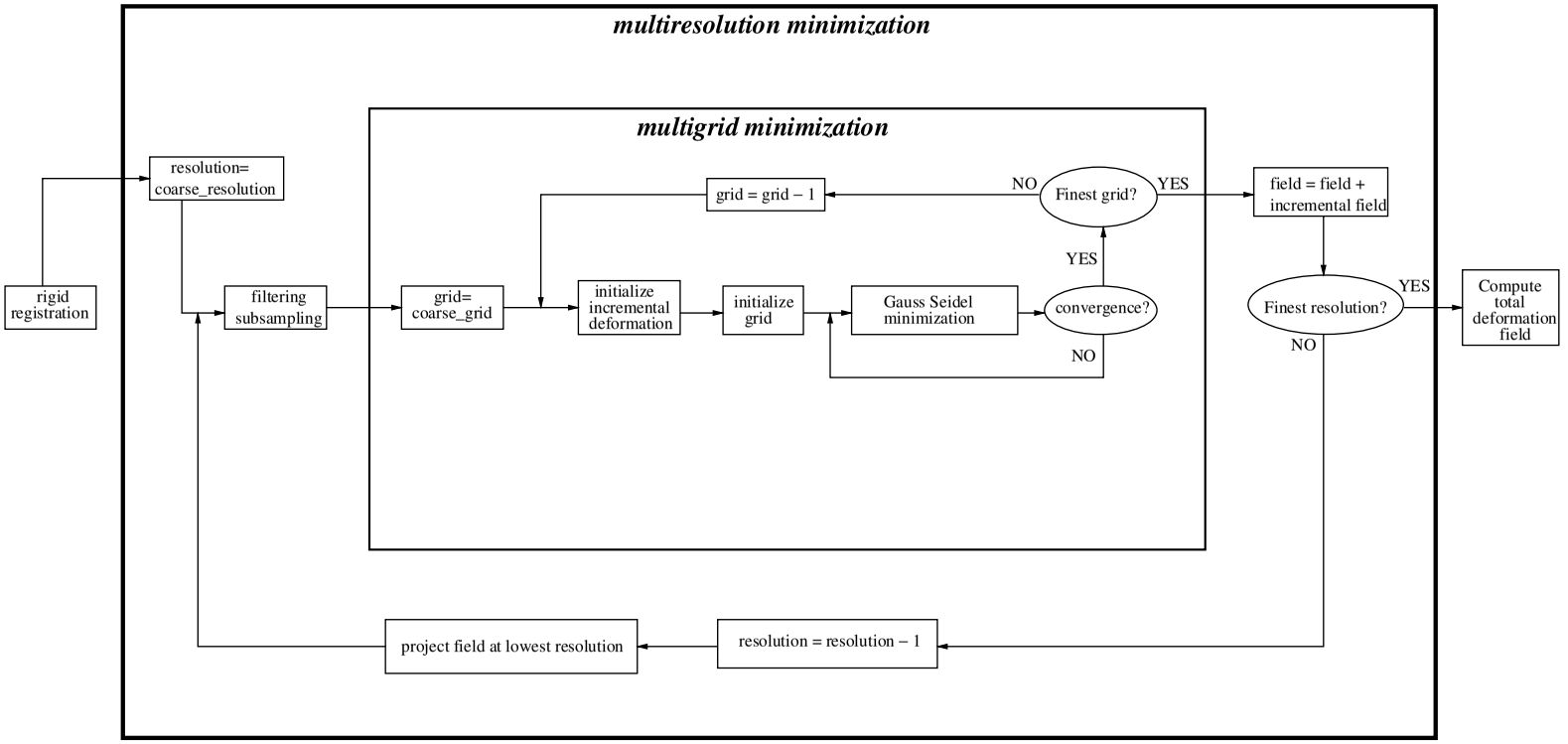

Figure 8.3: Overview of the multiresolution and multigrid minimization. The convergence of the multigrid minimization is based on a percentage of cubes for which the parametric incremental field has been updated (percentage of the total number of cubes of the image partition).

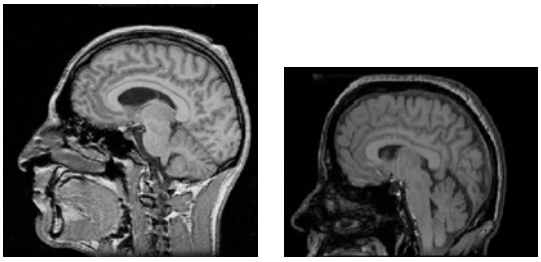

Source MR image **Target MR image**

Figure 8.4: MR images of different subjects. The intensity of tissue classes is different for source (top) and target (bottom) volume.

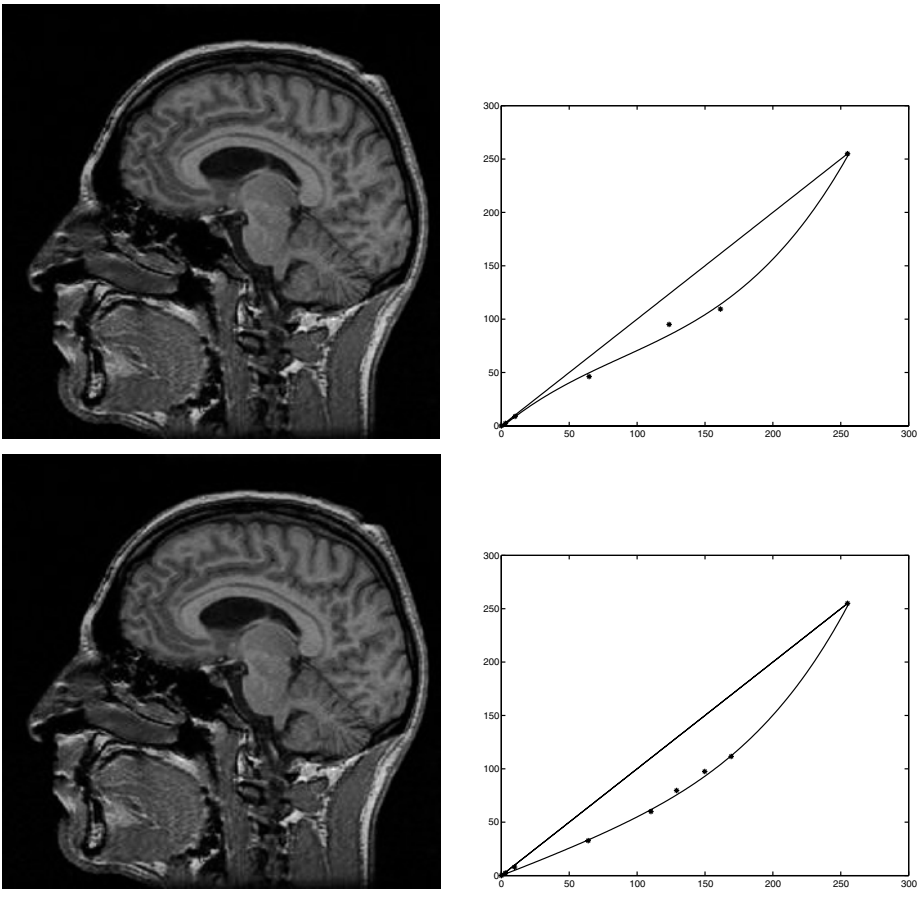

Figure 8.5: Intensity correction using the expectation maximization (EM) algorithm. The corrected source volume is presented, as well as the parametric intensity correction (to be compared with the identity function). The histogram has been modeled by five Gaussian distributions (top) and seven Gaussian distributions (bottom). Points represent the mean of Gaussian laws that model the histogram.

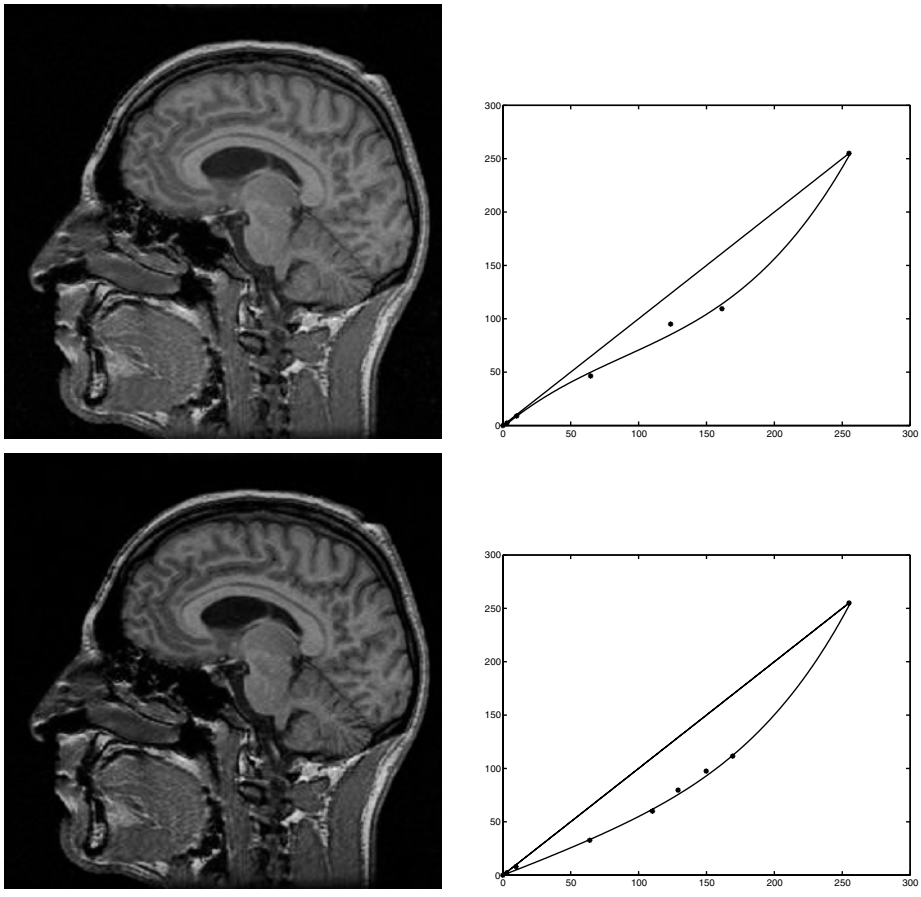

Figure 8.6: Intensity correction using the stochastic expectation maximization (SEM) algorithm. The corrected source volume is presented, as well as the parametric intensity correction (to be compared with the identity function). The histogram has been modeled by five Gaussian distributions (top) and seven Gaussian distributions (bottom). Points represent the mean of Gaussian laws that model the histogram.

Corrected source volumes and parametric correction functions are presented. The corrected volume seems visually more similar to the target volume (when comparing intensities of corresponding tissues). Modeling the histogram with seven classes seems more adequate in this context. This is actually more relevant from an anatomical point of view and provides more sample to estimate the correction function. The experiments we have conducted so far do not

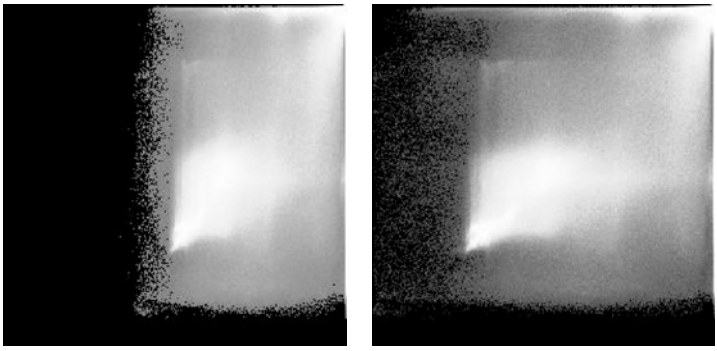

Before correction **After correction**

Figure 8.7: Joint histogram before and after intensity correction. To compute the joint histogram, MR volumes have been previously rigidly registered by maximizing mutual information [88].

favor the SEM or the EM algorithm. There may be an indication that the SEM is more adapted in presence of field inhomogeneity and should be investigated further.

The relevance of this intensity correction can be assessed using the joint histogram (Fig. 8.7). To compute the joint histogram, a spatial alignment of the volumes needs to be performed. To do so, we estimate a rigid displacement that maximizes mutual information [88]. Figure 8.7 shows the joint histogram before and after intensity correction (using EM and seven Gaussian laws to model the histogram). It must be noted that the same displacement has been applied to the corrected and uncorrected volume (in other words, the effect of a possible misalignment is equal for both histograms). The joint histogram shows the relevance of the intensity correction.

8.3.3.2 Experiments on Simulated Data

Evaluation on the MNI Phantom. To evaluate the global registration method, we use the simulated data provided by the MNI[3] [34]. Data have been collected with three levels of noise and inhomogeneity. We design a synthetic deformation field made up of a global affine field with large deformations combined with local stochastic perturbations. We do not try to build a "realistic"

[3] Brainweb: http://www.bic.mni.mcgill.ca/brainweb

field, but rather a field with the following properties: large deformations and local perturbations that modify the topology of the structures, in order to validate the basic hypothesis of our work. The "local" field is generated from 2,000 voxels which are randomly picked in the volume. For each voxel, each of the three components of the deformation is the realization of a Gaussian random variable of standard deviation 120 mm. We then perform a Gaussian smoothing with a small average deviation in order to propagate this perturbation to a local neighborhood while preserving discontinuities. The volumes and the results are shown on Fig. 8.8. We compare the multigrid method with a global affine registration method, in which a 12-parameter deformation is estimated for the entire volume.

To asses the quality of the registration, we compute the mean square error (MSE)[4] which is an indicator of the quality of the registration. However, it would be unfair to evaluate the registration only with a measure that is the underlying driving force of the estimation. Therefore, as we have the binary classification of the phantom, we can also assess the quality of the registration based on the overlap of two volumes: the first volume is the initial classification, i.e., a gold standard (gray matter/white matter), the second volume is the deformed classification, registered with the estimated deformation field. We then measure out overlapping ratios like the sensitivity, the specificity, and the total performance [142]. Results are presented in Table 8.1. Despite the use of binary classes, the resulting measures that we obtain are very satisfactory. Particularly, the robustness of the method is demonstrated in critical conditions (9% noise and 40% inhomogeneity), which are far tougher than in any realistic acquisition.

The numerical evaluation also allows to study the sensitivity of the algorithm with respect to the parameters of the algorithm, i.e., parameters of the robust estimators. We have two parameters to fix, σ_1 and σ_2. σ_1 corresponds to the hyperparameter of robust function ρ_1, associated with the similarity term, while σ_2 corresponds to the hyperparameter of robust function ρ_2 associated with the regularization term. We made the parameters σ_1 and σ_2 vary in a cube of size $[1.0e^4, 1.0e^5] \times [1, 20]$ with step, respectively, of $1.0e^4$ and 1 (which means that we performed the registration with 200 different sets of parameters), and we observe that the final result (the mean square error between the source volume

[4] $MSE = \frac{1}{N} \sum_{i=1}^{i=N} (I_1(i) - I_2(i))^2$, where I_1 and I_2 are the volumes to compare, and N is the number of voxels.

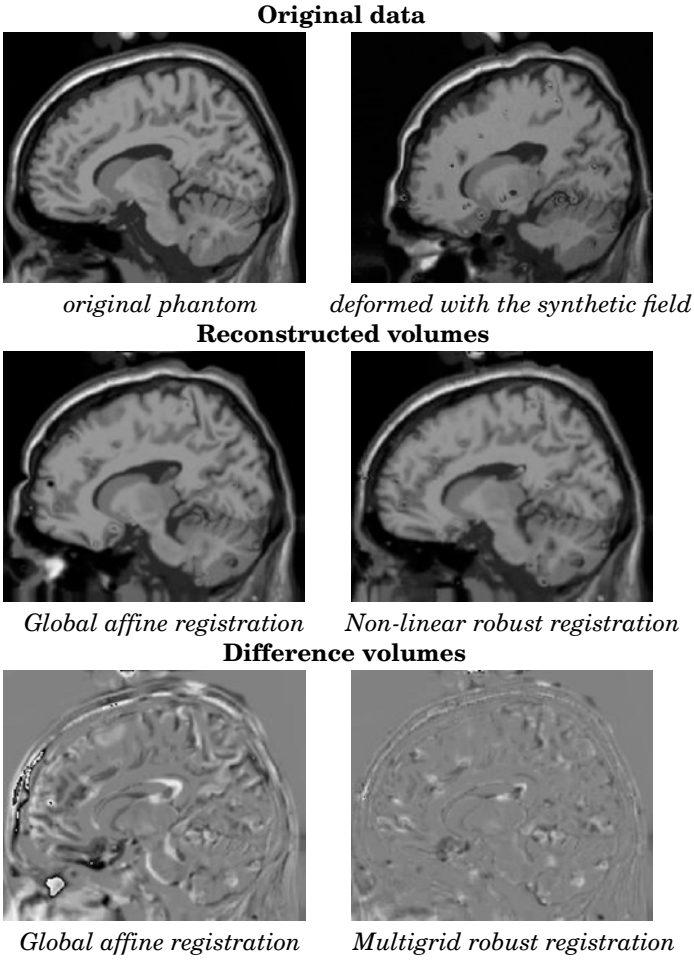

Figure 8.8: Results of the registration process on simulated data. The 3D MRI phantom has been deformed on the top of the figure. In the middle, the reconstructed volumes are shown and must be compared with the initial volume to evaluate the quality of the registration. On the bottom, the difference volumes show the benefits of non-linear registration.

and the reconstructed volume) varies less than 5% of the nominal MSE. This indicates that the sensitivity of algorithm with respect to these two parameters is very low.

For simulated data, mean square error (MSE) is a direct measure of the quality of the registration. Therefore we can also evaluate the influence of ℓ_f (see section 8.3.2) on the computation time and on the accuracy of the registration.

Table 8.1: Objective measures of the quality of the registration on simulated data. Specificity, sensitivity and total performance measures are given for three levels of noise and two registration methods. The registration processes are performed until resolution 0 (voxel size 1 mm^3). We manage to recover up to 93% of the deformation even in presence of important noise (9%) and image intensity inhomogeneity (40%). The CPU times are given for an Ultra Sparc at 333 Mhz

		Noise Inhomogeneity Target volume	0% 0% Grey matter	White matter	Noise Inhomogeneity Target volume	3% 20% Grey matter	White matter	Noise Inhomogeneity Target volume	9% 40% Grey matter	White matter
	Computation time	10′			10′			10′		
	MSE	964.63	2679.49	1751.41	1104.22	3305.50	2171.13	2005.14	6933.05	5031.49
Global	sensitivity		93.78%	91.19%		93.26%	89.01%		83.21%	77.33%
affine	specificity		93.16%	93.72%		91.69%	92.48%		83.19%	85.42%
	total performance		93.27%	93.41%		91.97%	92.06%		83.19%	85.42%
	Computation time	55′			61′			76′		
	MSE	138.57	1383.46	886.53	233.23	1534.48	970.42	667.88	3186.49	1463.87
Robust	sensitivity		97.83%	97.35%		97.09%	96.36%		95.50%	93.27%
multigrid	specificity		94.28%	94.35%		94.76%	94.90%		90.73%	93.67%
	total performance		94.91%	94.71%		95.35%	95.03%		91.50%	93.80%

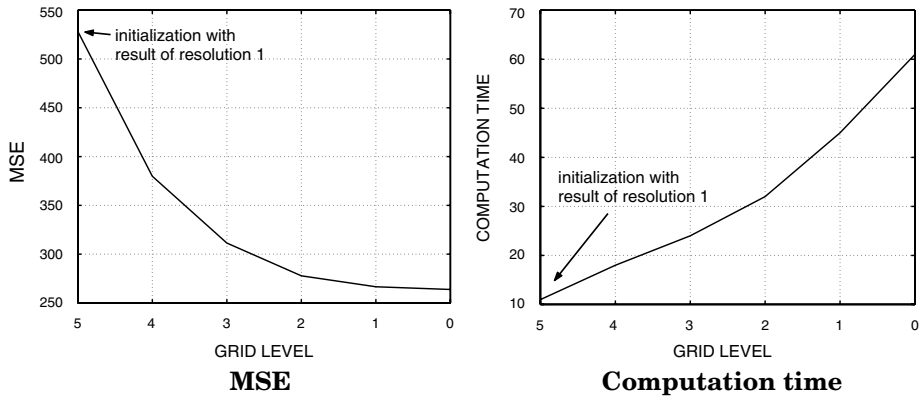

MSE **Computation time**

Figure 8.9: Evolution of the MSE with respect to the grid level (at finest resolution 1 mm) and computation time needed to perform the registration until a given grid level. We observe that the MSE decreases significantly at the coarsest grid level, whereas at the finest grid level it continues to decrease, but less rapidly. At the same time, the computation time increases continuously. If we look at the difference between grid level 2 (the smallest cubes are of size $2^2 \times 2^2 \times 2^2$ and the incremental deformation field is affine on each cube) and grid level 0 (the smallest cubes are reduced to a voxel and the incremental deformation field is translational for the smallest cubes), the computation time increases by 100%, whereas the MSE variation is only 5.3%. That suggests that, depending on the application, the user can make a compromise between the accuracy of the registration and the computation time if the resources are limited.

Figure 8.9 shows the evolution of the MSE with respect to the grid level (at finest resolution 1 mm) and also shows the computation time needed to perform the registration until a given grid level. We observe that the MSE decreases significantly at coarsest grid level, whereas at the finest grid level it continues to decrease, but less rapidly. At the same time, the computation time increases continuously. If we look at the difference between grid level[5] 2 and grid level[6] 0, the computation time increases by 100%, whereas the MSE variation is only 5.3%. That suggests that, depending on the application, the user can make a compromise between the accuracy of the registration and the computation time

[5]The smallest cubes are of size $2^2 \times 2^2 \times 2^2$ and the increment deformation field is affine on each cube.

[6]The smallest cubes are reduced to a voxel and the increment deformation field is translational for the smallest cubes.

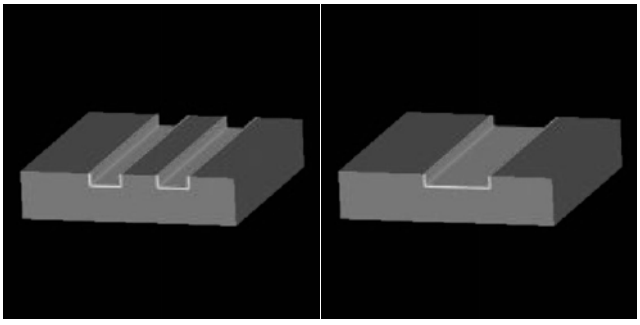

Source volume **Target volume**

Figure 8.10: Synthetic data to validate the link between robust estimator on the regularization term and local changes of topology.

if its resources are limited. In our case, we find that $\ell_f = 1$ (the smallest cubes are of size $2 \times 2 \times 2$ and the allowed deformation is rigid on the smallest cube) is generally a good compromise.

Importance of Robust Estimator. We have introduced robust estimators in the registration process, in order to let local discontinuities of the deformation field occur. We now want to verify on simulated data the direct link between the introduction of a robust function and the possibility to locally change the topology of the structures. Therefore, we construct two volumes (see Fig. 8.10) to be registered, with a local modification of the topology. The volumes are composed of two homogenous classes, each one being defined by a unique gray level. With these two volumes, we obviously face the aperture problem, which is classical in the optical flow literature.

We first register the two volumes without any robust estimator. Results are presented in Fig. 8.11. The reconstructed volumes are computed with the target volume and the estimated deformation field with trilinear interpolation. One must therefore compare the reconstructed volume and the source volume to assess the quality of the registration. The different volumes shown in Fig. 8.11 correspond to different values of the parameter α. This parameter balances the importance of the similarity term and the regularization term. When this parameter is high, the solution is smooth but the topology is not modified. When α decreases, the solution is not smooth, the aperture problem is obvious, whereas the topology is not correctly modified.

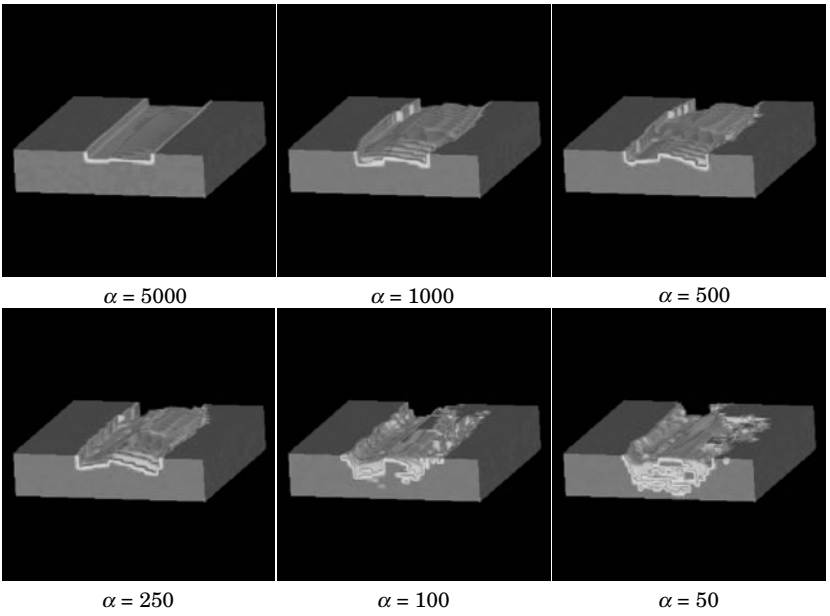

Figure 8.11: Results of the registration without robust estimator. The different volumes correspond to different values of the parameter α, and must be compared to the source volume.

We then perform the robust multigrid registration process, with a robust function only on the regularization term. Results are presented in Fig. 8.12, with two "extreme" values of the parameter α. In that case, the modification of the topology is possible, while preserving the global smoothness of the solution. However, the aperture problem is still present in the tubular structure on the right. This experiment makes it possible to verify the link between the introduction of a robust estimator on the regularization term and the possibility to handle local change of topology. In addition, the robust registration process appears to be also more robust with respect to the parameter α, because the results of the registration are very similar, when α varies in a range of [100, 3,000].

8.3.3.3 Experiment on Two Subjects

Importance of Intensity Correction. We first want to present cases where the registration method cannot work properly without a prior intensity

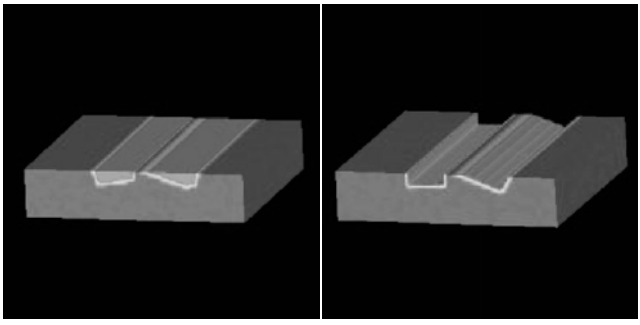

$\alpha = 100$ $\alpha = 3000$

Figure 8.12: Results of the registration with a robust estimator on the regularization term. The reconstructed volumes must be compared to the source volume. We can handle with local topology changes, while preserving the global smoothness of the solution.

correction. Figure 8.13 shows the impact of the intensity correction step on the registration of two volumes. The source image is first corrected using the EM algorithm, seven classes to model the histogram and a fourth order parametric correction. Figure 8.13 presents the source image deformed toward the target image, as well as the difference image. While the registration has failed without intensity correction due to a very large intensity difference, it has performed successfully with an intensity correction step. It must be noted that the set of parameters is the same for both registration processes. That demonstrated the usefulness of such correction for a non-rigid registration task.

Extensive Results for Two Subjects. Results of the 3D method are presented in Figs. 8.14, 8.15, and 8.16. Two 3D MRI-T1 volumes of two different subjects are registered. The source volume, the target volume and the reconstructed volume are presented in Fig. 8.14. The reconstructed volume $f_2(s + \hat{\boldsymbol{w}}_s)$ is computed with the target volume f_2 and the final displacement field $\hat{\boldsymbol{w}}$ by the way of a trilinear interpolation. To assess the quality of the registration, one must compare the source volume with the reconstructed volume.

We also present the volumes of difference, before and after registration in Fig. 8.15. In the same figure, the adaptive partition at grid level 3 is also presented (we do not present further grid levels for readability reasons). The difference volumes must be interpreted carefully, since we get the superposition of two

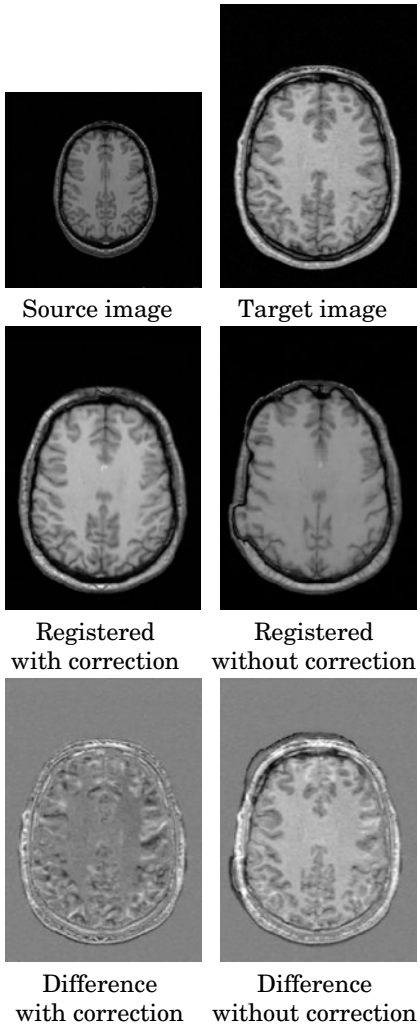

Figure 8.13: Impact of the intensity correction for the non-rigid registration. Top row: the images to be registered. Middle row: The source image is registered toward the target image, without intensity correction (left) and with correction (right). Bottom row: the differences images show the relevance of the intensity correction on the non-rigid registration.

errors: the first one is the registration error which comes from the anatomical variability that we could not apprehend. The second error is due to the difference of acquisition of the two volumes, which makes the histograms of the source and target volumes different.

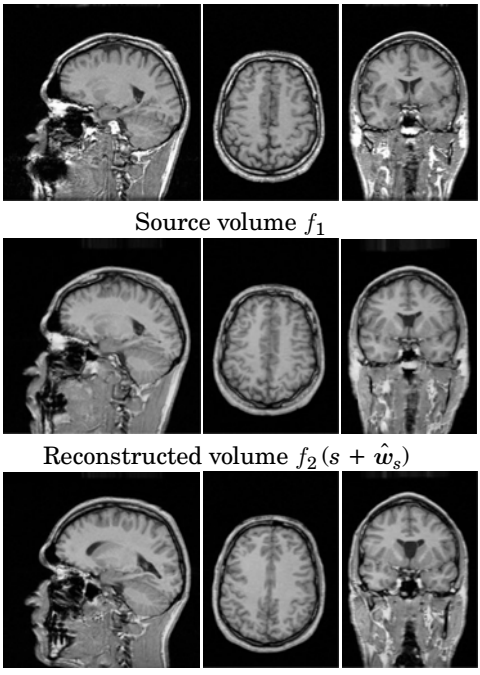

Figure 8.14: Final 3D results of the registration on real data. The volumes are T1-MRI acquisitions of two different subjects. The reconstructed volume is computed by trilinear interpolation with the target volume and the final dense displacement field. In order to evaluate the quality of the registration, we must therefore compare the source volume and the reconstructed volume.

In Fig. 8.16, the outliers are drawn, i.e., the data outliers map (variable δ_s) and the spatial outlier map (for each point s, we compute the mean of variable β_{sr} with respect to $r \in \mathcal{V}(s)$). Looking at the data outliers map, the dark points represent areas where the optical flow hypothesis is inadequate, because of occlusions for instance (see the jaw in Fig. 8.16). For these points, the regularization term overwhelms the similarity term. Looking at the spatial outlier term, we observe that dark regions are located in the cortex. At that locations, the importance of the regularization term is reduced, and discontinuities can appear. The fact that discontinuities appear in the cortex is significant because we know that inter-subject variability is very high on the cortex.

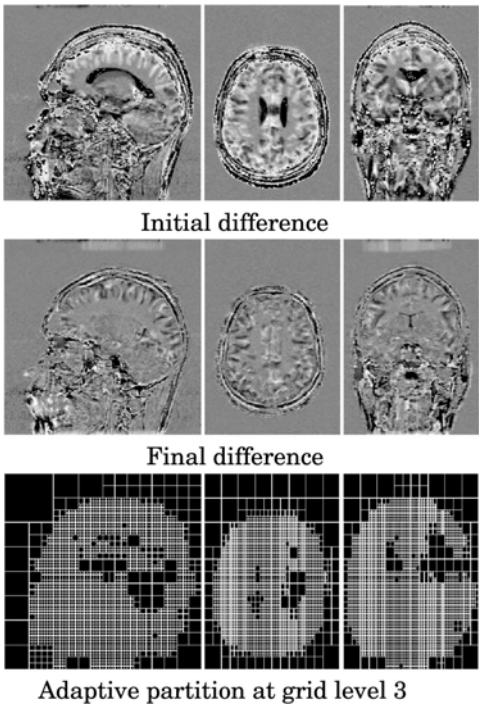

Figure 8.15: Final 3D results of the registration on real data. Top: difference before registration. Middle: difference after registration. Bottom: adaptive partition at grid level 3. The difference volumes must be interpreted carefully, since we get the superposition of two errors: the first one is the registration error which comes from the anatomical variability that we could not apprehend. The second error is due to the difference of acquisition of the two volumes, which makes the two original histograms of the two volumes different.

The 3D deformation field is presented in Fig. 8.17. The vector field is subsampled in order to be easier to look at, and we also show the three components of the field on the sagittal view. Although discontinuities are visible, the general spatial coherence of the final deformation field is visible, due to the regularization. The field also confirms that there is no "block-effect" in the registration process.

The computation takes about 1 : 30 hour on an Ultra Sparc 30 (300 MHz). The volumes are $256 \times 256 \times 200$. We use three levels of resolution ($k = 0, 1, 2$) because the displacement amplitude may reach 30 voxels, and at each resolution level we perform the registration from grid level 4 until grid level 0.

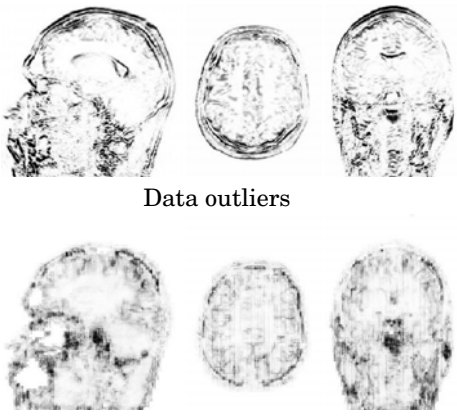

Figure 8.16: Final 3D results of the registration on real data. Top: data outlier map. Middle: spatial outlier map. Looking at the spatial outlier term, we observe that dark regions are located in the cortex. Dark areas shows that the importance of the regularization term is reduced, and discontinuities can appear. The fact that discontinuities appear in the cortex is significant because we know that inter-subject variability is very high on the cortex.

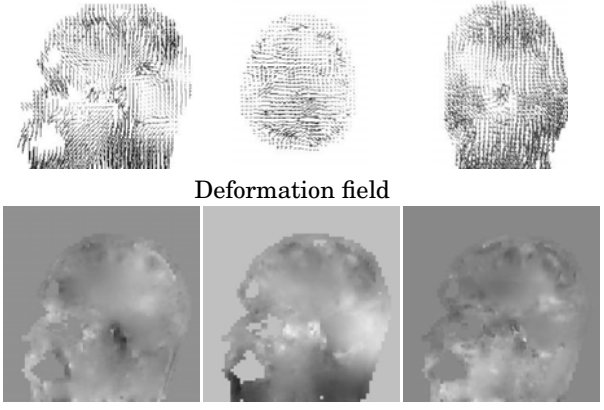

Figure 8.17: Top: deformation field. Bottom: Images of the three components of the field on the sagittal view. The 3D deformation field is subsampled in order to be easier to look at. Although discontinuities are visible, the general spatial coherence of the final deformation field is visible, due to the regularization. The field also confirms that there is no "block-effect" in the registration process.

8.3.3.4 Experiments on a Dataset of 18 Subjects

In order to validate the registration method on a larger database, we acquire MRI-T1 volumetric data of 18 patients. One subject is chosen as the reference subject. We then perform the registration between the reference volume (source) and each of the other subjects (target) using *always* the same set of parameters for the algorithm. Finally, we get 17 reconstructed volumes that can be compared to the reference volume. We average all the reconstructed volume in order to have a global overview of the quality of the method.

Average Deformed Volume. Figures 8.18 and 8.19 present the averaging between 17 patients after a global affine registration (top), after a quadratic multigrid registration, i.e., the method without robust estimators (middle), and the average volume after a robust multigrid registration (bottom). After global affine registration and averaging, we notice that the internal anatomical structures are blurred, because the registration is not precise enough. However, after a robust multigrid registration, we may distinguish precisely the contours of anatomical structures, such as ventricles, deep nuclei, white matter tracks, and even cortical regions (sylvian fissure and parietal region for instance).

The comparison between the quadratic registration and the robust registration shows the benefit of robust functions, because cortical regions are better registered. The MSE between the reference volume and the averaged volume is 892 for quadratic registration, and drops to 584 for robust registration. We must note that, considering two subjects, the MSE is not a good absolute measure of the quality of the registration because of the acquisition (a simple translation between the two histogram can lead to large MSE). However, the MSE is a good relative measure to compare two registration processes over a large database.

These experiments clearly show the significant impact of robust estimators. All the more, it validates the assumption that it is necessary to let discontinuities appear in the deformation field to register brains correctly. These experiments also demonstrate the robustness of the method (robustness with respect to the acquisitions and also with respect to the algorithm parameters) over a realistic database of subjects.

Overlapping of Brain Tissues. The evaluation must not be based only on a measure that is more or less related to the image similarity. Therefore, as in

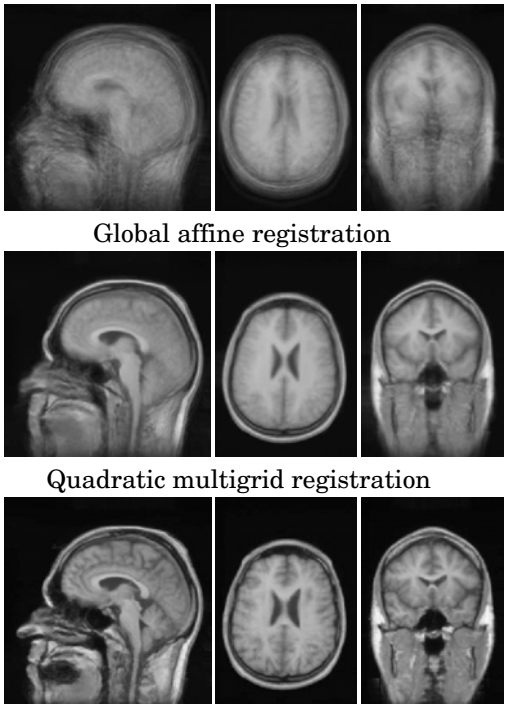

Figure 8.18: Results of experiments on a database of 18 subjects. One subject was chosen as the reference subject (see Fig. 8.19), and we averaged all the reconstructed volumes after global affine registration (top), after quadratic multigrid registration (middle) and after robust multigrid registration (bottom). We kept the same set of parameters for all the subjects. This demonstrates the robustness of the method, and the importance of robust estimators (the quadratic registration is less accurate on the cortex).

section 8.3.3, we evaluate in this section the registration process by computing the overlap between the tissues (gray matter and white matter) of the reference volumes and the tissues of each studied volume after registration. We measure the overlap with the total performance, which has already been presented in section 8.3.3.

The extraction of gray matter and white matter is performed using a technique presented in [85]. It consists in a 3D texture analysis to compute statistical attributes of each voxel. A clustering procedure is used to find the initial discrimination of the data, and a bayesian relaxation refines the primary decision.

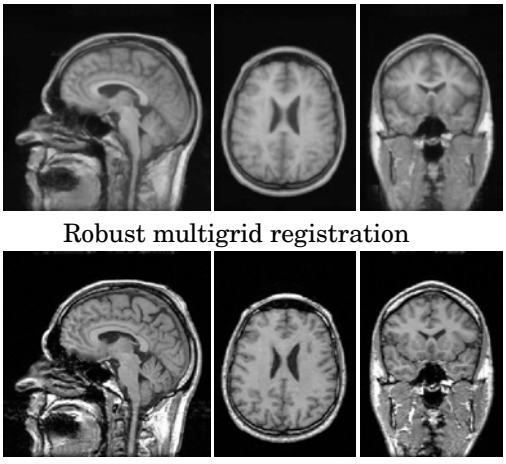

Figure 8.19: Results of experiments on a database of 18 subjects. One subject was chosen as the reference subject (bottom), and we averaged all the reconstructed volumes after robust multigrid registration (top). We kept the same set of parameters for all the subjects, which demonstrates the robustness of the method. Results of the averaging after registration show the accuracy of the registration (after averaging we can distinguish precisely anatomical structures such as ventricles, deep nuclei, white matter tracks and even cortical regions).

For gray matter tissue, the average overlap after registration is 93.9% (mean of total performance). For white matter, the average overlap is 94.9%. If we perform a rigid registration by maximization of mutual information, we obtain 88.3% and 87.1% of average overlap, for gray matter and white matter, respectively. These measures must be interpreted carefully for two reasons. We use binary classes (and not fuzzy classes) and a simple trilinear interpolation scheme, which may introduce some error. Furthermore, the classification algorithm introduces errors that disturb the overlapping measure. In the last 5% to recover, it is difficult to distinguish what is due to the registration process and what is due to interpolation and segmentation errors. However, these overlapping measures show the benefit of non-rigid registration.

8.3.3.5 Experiments on Multimodal Datasets

The extension of Romeo to multimodal dataset was motivated by a particular problem: the correction of distortions in echo-planar images. Among the

functional images of the brain, fMRI is an appealing technique because it offers a good trade-off between spatial and temporal resolution. To increase its temporal resolution, echo-planar imaging (EPI) is used because it makes possible to collect at least five slices per second at a reduced spatial resolution. The drawback of this impressive acquisition rate is that it may introduce artifacts and distortions in the data. More details about these distortions can be found in [78].

If the distortions do not vary during the time series, they will not affect much the detection of subtle signal changes, but they will perturb the localization of the functional activity once being overlapped to the anatomical volume. It becomes necessary to correct these geometrical distortions in order to accurately identify activated areas.

Simulated Data. To evaluate the multimodal registration method, we use the simulated database of the MNI (Brainweb)[7] [34]. The T1-weighted MR volume is the reference volume (3% noise and 9% inhomogeneity), whereas the T2-weighted MR volume is the floating volume.

From the T2-weighted MR volume, we extract a subvolume and we apply a rigid transformation (three rotations and three translations). To simulate local geometrical distortions, we apply a thin-plate spline [16] deformation to the volume. The thin-plate deformation is computed by choosing one point in the volume and a displacement for this point. We choose a displacement of magnitude 5 voxels, with no privileged direction. Furthermore, the thin-plate deformation field is constrained to be naught at the border of the volume.

After rigid registration (see Fig. 8.20), distortions are clearly visible. On the axial view, ventricles are not well registered ; on the sagittal and coronal view, the sagittal mid-plane is not well aligned. We then perform the multigrid non-rigid registration from grid level 7 until grid level 5 to avoid useless computational efforts. In this case we do not need to estimate a dense transformation, since the distortions are rather smooth and regular. Furthermore, the statistical similarity measure is only meaningful for a large number of voxels, i.e., for large cubes. After non-rigid registration, the internal structures are accurately registered (see ventricles on the axial view, and sagittal mid-plane on the coronal view for instance).

[7] http://www.bic.mni.mcgill.ca/brainweb

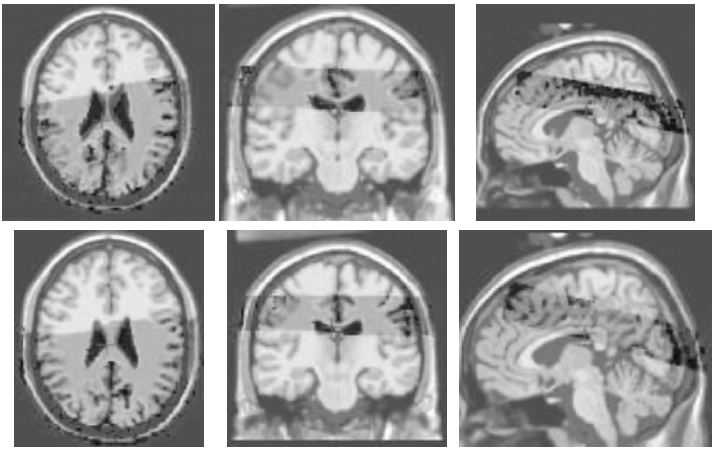

Figure 8.20: Results of the registration on simulated data. Top: results after rigid registration. Distortions are visible on axial view (ventricles) and on coronal view (sagittal mid-plane). Bottom: results after performing a 3D multimodal non-rigid registration. Misregistration is significantly reduced (see ventricles on axial view for instance).

In Fig. 8.21, we present the evolution of the similarity measure, computed for all the volume. As the hierarchical estimation is performed, the similarity increases, which means that the dependence between the volumes to be registered also increases, leading to a more and more accurate registration. This is a numerical confirmation of visual assessment.

At this stage, the evaluation is not completely fair, since the criterion is related to the similarity used to drive the registration process. As we have the segmentation of the phantom (gray matter and white matter classes), we can evaluate objectively the registration process. We deform the segmentation volumes as described at the beginning of section (8.3.3). We can assess the quality of the registration by computing overlapping measures (specificity, sensitivity and total performance, see [142] for tutorial) between the initial classes and the deformed classes, once registered with the estimated deformation field. Let us recall that:

$$\begin{cases} \text{sensitivity} & = TP/(TP+FN) \\ \text{specificity} & = TN/(FP+TN) \\ \text{total performance} & = (TP+TN)/(TP+FP+TN+FN), \end{cases} \tag{8.6}$$

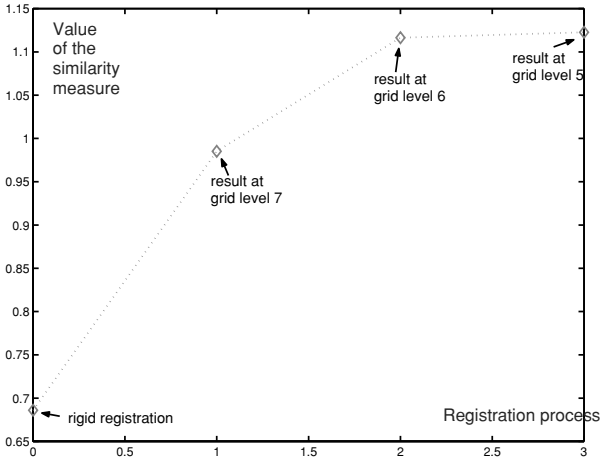

Figure 8.21: Evolution of the similarity measure. As the hierarchical estimation is performed, the similarity increases, which means that the volumes are more accurately registered.

where TP, TN, FP and FN, respectively, denote the number of true positive, true negative, false positive, and false negative points.

These numerical results are shown in Table (8.2). At the end of grid level 5, we manage to recover more than 95% of the segmentation. This result is satisfactory, due to the use of binary classes, and due to a simple trilinear interpolation scheme that causes artefacts [108].

Real Data. We have performed the algorithm on real data (see Fig. 8.22). The patient has a cyst and a bone tumor, therefore the multiple interfaces (air/cyst/bone) introduce large distortions that are visible after rigid registration. For instance, on the left hemisphere, distortions are clearly visible on the posterior part of the cyst.

There are many artefacts in this fMRI acquisition: there has been signal saturation and signal drops (visible in the cyst and in the border of the skull). This illustrates the difficulty of registering real clinical data. Although quality of the results is quite difficult to quantify, we can see that the cyst (on the axial view) and the ventricles (on the sagittal view) are better aligned after non-rigid registration.

Table 8.2: Numerical evaluation of the multimodal registration method on simulated data. The overlapping measures (specificity, sensitivity, and total performance) are computed after rigid registration and at each grid level of the non-rigid registration process

Registration	Overlap measure	Grey matter	White matter
Rigid	sensibility	74.7%	76.6%
	specificity	93.0%	92.8%
	Total performance	87.0%	87.6%
Non-rigid	sensibility	84.7%	86.0%
grid level 7	specificity	97.2%	96.2%
	Total performance	93.2%	92.9%
Non-rigid	sensibility	86.6%	86.8%
grid level 6	specificity	98.5%	97.3%
	Total performance	94.6%	93.9%
Non-rigid	sensibility	87.5%	87.0%
grid level 5	specificity	98.9%	98.0%
	Total performance	95.8%	95.3%

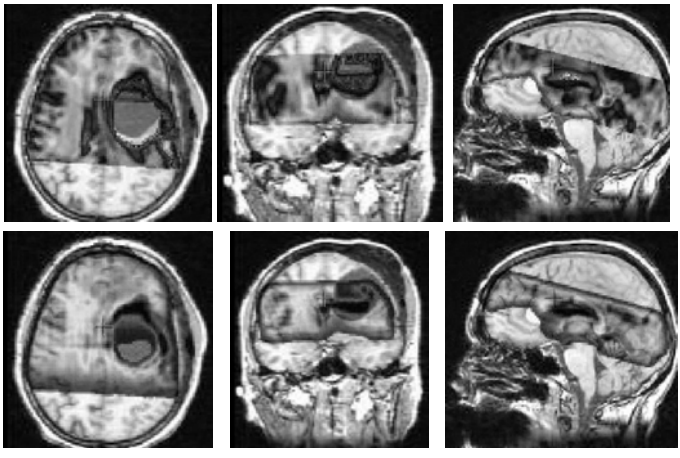

Figure 8.22: Results of clinical data. Top: results of the rigid registration. The multiple artefacts are visible: distortions, signal saturation, signal drops. Bottom: Results of the non-rigid registration. The registration is more accurate, in particular, for the ventricles and for the cyst. The data are courtesy of "laboratoire IDM, Hopital de Pontchaillou, Rennes".

8.4 Conclusion

This chapter has presented an overview of the classification of non-rigid registration methods with particular focus on non-rigid registration of brains of different subjects. Methods can be broadly classified into two groups: geometric methods that rely on the extraction and matching of sparse features (points, curves, surfaces), and photometric (or intensity-based) methods that rely on image luminance directly.

Geometric methods reduce the dimensionality of the problem and are consistent in the vicinity of features used for registration. However, the registration might be incorrect far from used features. Photometric methods use all the available information present in the volume but lead to a complex problem involving a very large number of variables.

We have presented here the Romeo algorithm (Robust Multigrid Elastic registration based on optical flow) that refers to photometric methods. Romeo uses the optical flow as a similarity measure and relies on an efficient multiresolution and multigrid optimization scheme. Robust estimators are introduced to limit the effect of erroneous data and to preserve discontinuities of the deformation field when needed. Prior to the non-rigid registration step, two preprocessing steps are performed: a rigid registration by maximization of mutual information and an intensity correction so that the luminance of the volumes to be registered are comparable. An extension to multimodal data has been presented. The multiresolution and multigrid framework is flexible enough to be adapted to multimodal similarity measures such as mutual information for instance.

It has been shown that photometric methods fail in matching cortical structures such as cortical sulci, for instance [74]. This can be explained by the high variability of cortical structures among subjects. Anatomists have pointed out [103] that cortical sulci of different subjects are very different in shapes. This has motivated mixed approaches where a photometric registration method incorporates sparse anatomical structures so as to drive the registration process [22, 29, 36, 68, 73, 79, 141].

In this context, it must be noted that validation is difficult and should be investigated further. Validation of non-rigid registration methods on anatomical structures have been conducted [74, 119]. However, the impact of non-rigid

registration methods on functional data is still unknown. As a matter of fact, since these methods are dedicated to anatomical and functional normalization, it would be interesting to know how much of the intersubject functional variability can be understood and compensated by anatomical non-rigid registration. This is a challenging research subject that requires a better knowledge about the relationship between the anatomy of the brain and its functional organization.

Questions

1. *What are photometric and geometric registration methods? How can these methods be compared?*
2. *What is optical-flow?*
3. *What is the aperture problem? How can it be solved?*
4. *What are the advantages and drawbacks of optical-flow based registration?*
5. *What are robust estimators?*
6. *What are the advantages and drawbacks of robust M-estimators?*
7. *How useful is a multiresolution scheme?*
8. *How should the Gaussian standard deviation be chosen for building the multiresolution pyramid?*
9. *What is a multigrid optimization scheme?*
10. *What are the different options to regularize the deformation field?*

Bibliography

[1] Ashburner, J., Andersson, J., and Friston, K. J., Image registration using a symetric prior in three dimensions. Human Brain Mapping, Vol. 9, pp. 212–225, 1998.

[2] Ashburner, J. and Friston, K., Nonlinear Spatial Normalization using basis functions. Human Brain Mapping, Vol. 7, No. 4, pp. 254–266, 1999.

[3] Cuadra, M. Bach, Platel, B., Solanas, E., Butz, T., and Thiran, J. P., Validation of tissue modelization and classification techniques in T1-weighted MR brain images, In: Proc. of Medical Image Computing and Computer-Assisted Intervention, Dohi, T. and Kikinis, R., ed., No. 2488 In Lecture Notes in Computer Science, pp. 290–297, Springer, Tokyo, September 2002.

[4] Bajcsy, R. and Broit, C., Matching of deformed images, In: Proc. International Conference on Pattern Recognition, Vol. 1, pp. 351–353, IEEE, New York, Munich, West Germany, Oct. 1982.

[5] Bajcsy, R. and Kovacic, S., Multiresolution elastic matching, Computer Vision, Graphics, Image Processing, Vol. 46, pp. 1–21, 1989.

[6] Barr, A., Global and local deformations of solid primitives, Computer Graphics (SIGGRAPH), Vol. 18, no. 3, pp. 21–30, 1984.

[7] Barron, J., Fleet, D., Beauchemin, S., and Burkitt, T., Performance of optical flow techniques, In: Proc. Conference on Computer Vision Pattern Recognition, pp. 236–242, Champaign, Illinois, Jun. 1992.

[8] Bascle, B., Contributions et applications des modèles déformables en vision par ordinateur, Ph.D. thesis, Université de Nice Sophia-Antipolis, Sep. 1994.

[9] Battiti, R., Amaldi, E., and Koch, C., Computing optical flow over multiple scales: an adaptive coarse-to-fine strategy, International Journal of Computer Vision, Vol. 6, No. 2, pp. 133–146, 1991.

[10] Beauchemin, S. and Barron, J., The computation of optical flow, ACM Computing Surveys, Vol. 27, No. 3, pp. 433–467, 1995.

[11] Bergen, J., Anadan, P., Hanna, K., and Hingorani, R., Hierarchical model-based motion estimation, In: Proc. European Conference on Computer Vision, pp. 5–10, 1991.

[12] Besl, P. and McKay, N., A method for registration of 3D shapes, IEEE Trans. Pattern Analysis and Machine Intelligence, Vol. 14, No. 2, pp. 239–255, 1992.

[13] Black, M. and Anandan, P., The robust estimation of multiple motions: parametric and piecewise-smooth flow fields, Computer Vision and Image Understanding, Vol. 63, No. 1, pp. 75–104, 1996.

[14] Black, M. and Rangarajan, A., On the unification of line processes, outlier rejection, and robust statistics with application in early vision, International Journal of Computer Vision, Vol. 19, No. 1, pp. 57–91, 1996.

[15] Blake, A. and Isard, M., Active contours. Springer, 1998.

[16] Bookstein, F., Principal warps: Thin-plate splines and the decomposition of deformations, IEEE Transactions on Pattern Analysis and Machine Intelligence, Vol. 11, No. 6, pp. 567–585, 1989.

[17] Bro-Nielsen, M. and Gramkow, C., Fast fluid registration of medical images, In: Proc. Visualization in Biomedical Computing, Hohne, K-. H. and Kikinis, R., ed., No. 1131 In Lecture Notes in Computer Science, pp. 267–276, Springer, Sep. 1996.

[18] Broit, C., Optimal registration of deformed images, Ph.D. Dissertaition, Department of Computer and Information Science, University of Pennsylvania, Philadelphia, 1981.

[19] Brown, L. F., A survey of image registration techniques, ACM: Computer Surveys, Vol. 24, No. 4, pp. 325–376, 1992.

[20] Burt, J. P., Multiresolution image processing and analysis, Chapter 2 : The pyramide as a structure for efficient computation, pp. 6–38, No. 12 In Springer series in Information Science, Springer-Verlag, 1984.

[21] Cachier, P., Bardinet, E., Dormont, D., Pennec, X., and Ayache, N., Iconic feature based nonrigid registration: the PASHA algorithm, Computer Vision and Image Understanding, Vol. 89, No. 2/3, pp. 272–299, 2003.

[22] Cachier, P., Mangin, J. F., Pennec, X., Rivière, D., Papadopoulos-Orfanos, D., Régis, J., and Ayache, N., Multisubject non-rigid registration of brain MRI using intensity and geometric features, In: Proc. of Medical Image Computing and Computer-Assisted Intervention, Niessen, W. and Viergever, M., eds., No. 2208 in Lecture Notes in Computer Science, pp. 734–742, 2001.

[23] Celeux, G., Chauveau, D., and Diebolt, J., Stochastic version of the EM algorithm: an experimental study in the mixture context, Journal of Computationnal Statistical Computation and Simulation, Vol. 55, pp. 287–314, 1996.

[24] Charbonnier, P., Blanc-Féraud, L., Aubert, G., and Barlaud, M., Deterministic edge preserving regularization in computed imaging, IEEE Transactions Image Processing, Vol. 6, No. 2, pp. 298–311, 1997.

[25] Chen, C., Huang, T., and Arrott, M., Modeling, analysis and vizualisation of left-ventricule shape and motion by hierarchical decomposition, IEEE Transactions on Pattern Analysis and Machine Intelligence, Vol. 16, No. 4, 1994.

[26] Chen, G., Kessler, M., and Pitluck, S., Structure transfer between sets of three dimensionnal medical imaging data, In: VI Conference on Computer Graphics, Vol. 6, pp. 171–177, 1985.

[27] Christensen, G., Rabbit, R., and Miller, M. I., Deformable templates using large deformation kinematics, IEEE Transactions on Image Processing, Vol. 5, No. 10, pp. 1435–1447, 1996.

[28] Christensen, G. and Johnson, H. J., Consistent image registration, IEEE Transactions Medical Imaging, Vol. 20, No. 7, pp. 568–582, 2001.

[29] Chui, H., Rambo, J., Duncan, J., Schultz, R., and Rangarajan, A., Registration of cortical anatomical structures via robust 3D point matching, In: Proc. Information Processing in Medical Imaging, Cuba, *et al.*, ed., No. 1613 In: Lecture Notes in Computer Science, pp. 168–181, Springer Verlag, 1999.

[30] Chui, H. and Rangarajan, A., A new point matching algorithm for non-rigid registration, Computer Vision and Image Understanding, Vol. 89, No. 2/3, pp. 114–142, 2003.

[31] Cohen, I. and Herlin, I., Optical flow and phase portrait methods for environmental satellite image sequences, In: Proc. European Conference on Computer Vision, pp. II:141–150, Cambridge, UK, April 1996.

[32] Cohen, L. and Cohen, I., Finite element method for active contour models and ballons for 2D and 3D images, IEEE Transactions of Pattern Analysis and Machine Intelligence, Vol. 15, No. 11, pp. 1131–1147, 1993.

[33] Collignon, A., Vanderneulen, D., Suetens, P., and Marchal, G., 3D multi-modality medical image registration using feature space clustering, In: Proc. of Computer Vision, Virtual Reality and Robotics in Medecine, pp. 195–204, Nice, France, 1995.

[34] Collins, D. L., Zijdenbos, A. P., Kollokian, V., Sled, J. G., Kabani, N. J., Holmes, C. J., and Evans, A. O., Design and construction of a realistic digital brain phantom, IEEE Transactions on Medical Imaging, Vol. 17, No. 3, pp. 463–468, June 1998.

[35] Collins, L. and Evans, A., Animal : validation and applications of nonlinear registration-based segmentation, International Journal of Pattern Recognition Artificial Intelligence, Vol. 8, No. 11, pp. 1271–1294, 1997.

[36] Collins, L., Goualher, Le, G., and Evans, A., Non-linear cerebral registration with sulcal constraints, In: Proc. of Medical Image Computing and Computer-Assisted Intervention, Colchester, A. and Delp, S., eds., No. 1496 in Lecture Notes in Computer Science, pp. 974–985, Springer, October 1998.

[37] Corpetti, T., Mémin, E., and Pérez, P., Dense estimation of fluid flows, IEEE Transactions on Pattern Analysis and Machine Intelligence, Vol. 24, No. 3, pp. 365–380, 2002.

[38] Davatzikos, C., Spatial transformation and registration of brain images using elastically deformable models, Computer Vision and Image Understanding, Vol. 66, No. 2, pp. 207–222, 1997.

[39] Davatzikos, C., Prince, L., and Bryan, N., Image registration based on boundary mapping, IEEE Transactions on Medical Imaging, Vol. 15, No. 1, pp. 111–115, 1996.

[40] Dawant, B., Hartmann, S., Thirion, J. P., Maes, F., Vandermeulen, D., and Demaerel, P., Automatic 3D segmentation of internal structures of the head in MR images using a combination of similarity and free-form transformations: Part I, Methodology and validation on normal subjects, IEEE Transactions on Medical Imaging, Vol. 18, No. 10, pp. 909–916, 1999.

[41] Declerck, J., Subsol, G., Thirion, J. P., and Ayache, N., Automatic retrieval of anatomical structures in 3D medical images, In: Proc. of Computer Vision, Virtual Reality and Robotics in Medicine, Ayache, N., ed., No. 905 in LNCS, pp. 153–162, Springer, Nice, France, April 1995, Electronic version: ftp://ftp.inria.fr/INRIA/publication/RR/RR-2485.ps.gz.

[42] Delaney, A. and Bresler, Y., Globally convergent edge-preserving regularized reconstruction: an application to limited-angle tomography, IEEE Transanction Image Processing, Vol. 7, No. 2, pp. 204–221, 1998.

[43] Delingette, H., Hebert, M., and Ikeuchi, K., Shape representation and image segmentation using deformable models, Image and Vision Computing, Vol. 10, No. 3, pp. 132–144, 1992.

[44] Dempster, A. P., Laird, N. M., and Rubin, D. B., Maximum likelihood for incomplete data via the EM algorithm, Journal of the Royal Statistical Society, Vol. 39, pp. 1–38, 1977.

[45] Deriche, R., Recursively implementing the gaussian and its derivatives, Technical Report 1893, INRIA, http://www.inria.fr/RRRT/RR-1893.html, April 1993.

[46] Devlaminck, V., A functional for compressive and incompressive elastic deformation estimation, IEEE Signal Processing Letters, Vol. 6, No. 7, pp. 162–164, 1999.

[47] Duchon, J., Interpolation des fonctions de deux variables suivant le principe de la flexion des plaques minces, RAIRO Analyse Numérique, Vol. 10, pp. 5–12, 1976.

[48] Enkelmann, W., Investigations of multigrid algorithms for the estimation of optical flow fields in image sequences, Computer Vision, Graphics, Image Processing, Vol. 43, No. 2, pp. 150–177, 1988.

[49] Evans, A., Collins, L., and Milner, B., An MRI-based stereotaxic atlas from 250 young normal subjects, Society for Neuroscience Abstract, Vol. 18, pp. 408, 1992.

[50] Evans, A. C., Dai, W., Collins, D. L., Neelin, P., and Marrett, T., Warping of computerized 3D atlas to match brain image volumes for quantitative neuroanatomical and functionnal analysis, In: Proc. of the International Society of Optical Engineering: Medical Imaging V, SPIE, 1991.

[51] Feldmar, J. and Ayache, N., Locally affine registration of free-form surfaces, In: Proc. Conference on Computer Vision Pattern Recognition, pp. 496–500, Seattle, June 1994.

[52] Feldmar, J. and Ayache, N., Rigid, affine and locally affine registration of free-form surfaces, International Journal of Computer Vision, Vol. 18, No. 2, pp. 99–119, 1996.

[53] Feldmar, J., Declerck, J., Malandain, G., and Ayache, N., Extension of the ICP algorithm to nonrigid intensity based registration of 3D images, Computer Vision and Image Understanding, Vol. 66, No. 2, pp. 193–206, 1997.

[54] Ferrant, M., Warfield, S., Guttmann, C., Mulkern, R., Jolesz, F., and Kikinis, R., 3D image matching using a finite element based elastic deformation model, In: Proc. of Medical Image Computing and Computer-Assisted Intervention, Taylor, C. and Colchester, A., eds., No. 1679 in Lecture Notes in Computer Science, pp. 202–209, Cambridge, UK, September 1999.

[55] Friston, K. J., Ashburner, J., Frith, C. D., Poline, J. B., Heather, J. D., and Frackowiak, R. SJ., Spatial registration and normalisation of images, Human Brain Mapping, Vol. 2, pp. 165–189, 1995.

[56] Gabrani, M. and Tretiak, O., Surface-based matching using elastic transformation, Pattern Recognition, Vol. 32, pp. 87–97, 1999.

[57] Gaens, T., Maes, F., Vandermeulen, D., and Suetens, S., Non-rigid multimodal image registration using mutual information, In: Proc. of Medical Image Computing and Computer-Assisted Intervention, No. 1496 in Lecture Notes in Computer Science, pp. 1099–1106, October 1998. Springer Verlag, Boston.

[58] Gee, J., Briquer, Le, L., Barillot, C., and Haynor, D., Probabilistic matching of brain images, In: Proc. Information Processing in Medical Imaging, Bizais, *et al.*, ed., Kluwer Academic Publisher, Brest, Jun. 1995.

[59] Gee, J. C., Reivicj, M., and Bajcsy, R., Elastically deforming 3D atlas to match anatomical brain images, Journal of Computer Assisted Tomography, Vol. 17, No. 2, pp. 225–236, 1993.

[60] Gerlot, P. and Bizais, Y., Image registration: a review and a strategy for medical application, In: Proc. Information Processing in Medical Imaging, De Graaf, C. and Viergever, M., eds., pp. 81–89, Plenum Press, New York, 1988.

[61] Goshtasby, A., Staib, L., Studholme, C., and Terzopoulos, D., eds., Computer Vision and Image Understanding: Special issue on nonrigid image registration, Vol. 89 No. 2/3, Academic Press, February/March 2003.

[62] Keyserlingk, Graf von, D., Niemann, K., and Wasel, J., A quantitative approach to spatial variation of human cerebral sulci, Acta Anatomica, Vol. 131, pp. 127–131, 1988.

[63] Guimond, A., Roche, A., Ayache, N., and Meunier, J., Multimodal brain warping using the demons algorithm and adaptative intensity corrections, IEEE Transactions on Medical Imaging, Vol. 20, No. 1, pp. 58–69, 2001.

[64] Gupta, S. and Bajcsy, R., Volumetric segmentation of range images of 3D objects using superquadrics models, CVGIP: Image Understanding, Vol. 58, No. 3, pp. 302–326, 1993.

[65] Gupta, S. and Prince, J., On variable brightness optical flow for tagged MRI, In: Proc. Information Processing in Medical Imaging, Bizais *et al.*, ed, pp. 323–334, Kluwer Academic Publisher, Brest, June 1995.

[66] Guéziec, A. and Ayache, N., Smoothing and matching of 3D space curves, International Journal of Computer Vision, Vol. 12, No. 1, pp. 79–104, 1994.

[67] Hackbusch, W., Multigrid Methods and Applications, Springer Verlag, 1985.

[68] Hartkens, T., Hill, D., Castellano-Smith, A., Hawkes, D., Maurer, C., Martin, A., Hall, W., Liu, H., and Truwit, C., Using points and surfaces to improve voxel-based non-rigid registration, In: Proc. of Medical Image Computing and Computer-Assisted Intervention, Dohi, T. and Kikinis, R., eds., No. 2488 in Lecture Notes in Computer Science, pp. 565–572, Springer, Tokyo, September 2002.

[69] He, Renjie and Narayana, Ponnada A. Global optimization of mutual information: application to three dimensional retrospective registration of magnetic resonance images. Computerized Medical Imaging and Graphics, Vol. 26, No. 4, pp.277–292, 2002.

[70] Hebert, M. and Ikeuchi, H., K.and Delingette, A spherical representation for recognition of free form surfaces, IEEE Transactions on Pattern Analysis and Machine Intelligence, Vol. 17, No. 7, pp. 681–690, 1995.

[71] Hellier, P., Consistent intensity correction of MR images, In: IEEE conference on Image Processing, ICIP 2003, Barcelona, September 2003.

[72] Hellier, P. and Barillot, C., Multimodal non-rigid warping for correction of distortions in functional MRI, In: Proc. of Medical Image Computing and Computer-Assisted Intervention, MICCAI'00, Delp, S. *et al.*, ed., No. 1935 in Lecture Notes in Computer Science, pp. 512–521, Springer, Pittsburgh, Pennsylvania, October 2000.

[73] Hellier, P. and Barillot, C., Coupling dense and landmark-based approaches for non-rigid registration, IEEE Transactions on Medical Imaging, Vol. 22, No. 2, pp. 217–227, 2003.

[74] Hellier, P., Barillot, C., Corouge, I., Gibaud, B., Goualher, Le G., Collins, D. L., Evans, A., Malandain, G., Ayache, N., Christensen, G. E., and Johnson, H. J., Retrospective evaluation of inter-subject brain registration,

IEEE Transactions on Medical Imaging, Vol. 22, No. 9, pp. 1120– 1130, 2003.

[75] Hellier, P., Barillot, C., Mémin, E., and Pérez, P., Hierarchical estimation of a dense deformation field for 3D robust registration, IEEE Transactions on Medical Imaging, Vol. 20, No. 5, pp. 388–402, 2001.

[76] Horn, B. and Schunck, B., Determining optical flow, Artificial Intelligence, Vol. 17, pp. 185–203, August 1981.

[77] Huber, P., Robust Statistics, Wiley, 1981.

[78] Jezzard, P. and Clare, S., Sources of distortions in functional MRI data, Human Brain Mapping, Vol. 8, pp. 80–85, 1999.

[79] Johnson, H. J., and Christensen, G. E., Consistent Landmark and intensity-based Image registration, IEEE Transactions on Medical Imaging, Vol. 21, No. 5, pp. 450–461, 2002.

[80] Jones, R. and Witte, D., Signal intensity artefacts in clinical MR imaging, Radiographics, Vol. 20, pp. 893–901, 2000.

[81] Kikinis, R., Shenton, M., Iosifescu, D., McCarley, R., Saiviroonporn, P., Hokama, H., Robatino, A., Metcalf, D., Wible, C., Portas, C., Donnino, R., and Jolesz, F., A digital brain atlas for surgical planning, model driven segmentation and teaching, IEEE Transactions on Visualization and Computer Graphics, Vol. 2, No. 3, pp. 232–241, 1996.

[82] Konrad, J. and Dubois, E., Bayesian estimation of motion vector fields, IEEE Transactions on Pattern Analysis and Machine Intelligence, Vol. 14, No. 9, pp. 910–927, 1992.

[83] Kovacevic, N., Lobaugh, N. J., Bronskill, M. J., Levine, B., Feinstein, A., and Black, S. E., A robust method for extraction and automatic segmentation of brain images, Neuroimage, Vol. 17, pp. 1087–1100, 2002.

[84] Kybic, J., Thevenaz, P., Nirkko, A., and Unser, M., Unwarping of unidirectionally distorted EPI images, IEEE Transactions on Medical Imaging, Vol. 19, No. 2, pp. 80–93, 2000.

[85] Lachmann, F. and Barillot, C., Brain tissue classification from mri data by means of texture analysis, In: Medical Imaging VI: Image Processing, SPIE Press, ed., Vol. 1652, pp. 72–83, 1992.

[86] Leemput, K. V., Maes, F., Vandermeulen, D., and Suetens, P., Automated model-based tissue classification of MR images of the brain, IEEE Transactions on Medical Imaging, Vol. 18, No. 10, pp. 897–908, 1999.

[87] Lester, H. and Arridge, S., A survey of hierarchical non-linear medical image registration, Pattern Recognition, Vol. 32, pp. 129–149, 1999.

[88] Maes, F., Collignon, A., Vandermeulen, D., Marchal, G., and Suetens, P., Multimodality image registration by maximisation of mutual information, IEEE Transactions on Medical Imaging, Vol. 16, No. 2, pp. 187–198, April 1997.

[89] Maintz, J., Meijering, E., and Viergever, M., General multimodal elastic registration based on mutual information, In: Proc. of Medical Imaging: Image Processing, Hanson, M., ed., No. 3338 in SPIE Proceedings, pp. 144–154, San Diego, USA, April 1998.

[90] Maintz, J. and Viergever, M. A., A survey of medical image registration, Medical Image Analysis, Vol. 2, No. 1, pp. 1–36, 1998.

[91] Maurer, C. R., and Fitzpatrick, J. M., A review of medical image registration, In: Interactive Image Guided Neurosurgery, pp. 17–44, American Association of Neurological Surgeons, 1993.

[92] Mazziotta, J., Toga, A., Evans, A., Fox, P., and Lancaster, J., A probabilistic atlas of the human brain: theory and rationale for its development, Neuroimage, Vol. 2, pp. 89–101, 1995.

[93] McCormick, S., Multilevel Adaptive Methods for Partial Differential Equations, SIAM, Philadelphia, Pennsylvania, 1989.

[94] McInerney, T. and Terzopoulos, D., Deformable models in medical image analysis: A Survey, Medical Image Analysis, Vol. 1, No. 2, pp. 91–108, 1996.

[95] Meinguet, J., Multivariate interpolation at arbitrary points made simple, Journal of Applied Mathematics, Vol. 30, 1979.

[96] Metaxas, D. and Terzopoulos, D., Shape and nonrigid motion estimation through physics-based synthesis, IEEE Transactions on Pattern Analysis and Machine Intelligence, Vol. 15, No. 6, pp. 580–591, 1993.

[97] Miller, M. I., Christensen, G. E., Amit, Y., and Grenander, U., Mathematical textbook of deformable neuroanatomies, In: Proceedings of the National Academy of Sciences, Vol. 90, No. 24, pp. 11944–48, December 1993.

[98] Mémin, E. and Pérez, P., Dense estimation and object-based segmentation of the optical flow with robust techniques, IEEE Transactions on Image Processing, Vol. 7, No. 5, pp. 703–719, 1998.

[99] Mémin, E. and Risset, T., Vlsi design methodology for edge-preserving image reconstruction, Real-Time Imaging, 2000, Available at: http://www.irisa.fr/EXTERNE/bibli/pi/1220/1220.html.

[100] Monga, O., Ayache, N., and Sander, P., From voxel to intrinsic surface feature, Computer Vision and Image Understanding, Vol. 10, No. 6, pp. 403–417, 1992.

[101] Musse, O., Heitz, F., and Armspach, J. P., 3D deformable image matching using multiscale minimization of global energy functions, In: Proc. Conference Computer Vision Pattern Recognition, Vol. 2, pp. 478–485, Fort Collins, Colorado, June 1999.

[102] Odobez, J. M., and Bouthemy, P., Robust multiresolution estimation of parametric motion models, Journal of Visual Communication and Image Representation, Vol. 6, No. 4, pp. 348–365, 1995.

[103] Ono, M., Kubik, S., and Abernathey, C., Atlas of the Cerebral Sulci, Verlag, 1990.

[104] Peckar, W., Schnorr, C., Rohr, K., and Stiehl, S., Parameter-free elastic registration of brain images using prescribed displacements, Technical report, Universitat Hamburg Hachbereich Informatik, 1997.

[105] Peckar, W., Schnorr, C., Rohr, K., and Stiehl, S., Parameter-free elastic deformation approach for 2D and 3D registration using prescribed

displacement, Journal of Mathematical Imaging and Vision, Vol. 10, No. 2, pp. 143–162, 1999.

[106] Pennec, X., Cachier, P., and Ayache, N., Understanding the demon's algorithm : 3D non-rigid registration by gradient descent, In: Proc. of Medical Image Computing and Computer-Assisted Intervention, Taylor, C. and Colchester, A., eds., No. 1679 in Lecture Notes in Computer Science, pp. 597–605, Springer, Cambridge, UK, September 1999.

[107] Pentland, A. and Sclaroff, S., Closed-form solutions for physically-based shape modeling and recognition, IEEE Transactions on Pattern Analysis and Machine Intelligence, Vol. 13, No. 7, pp. 715–729, 1991.

[108] Pluim, J., Maintz, J., and Viergever, M., Interpolation artefacts in mutual information-based image registration, Computer Vision and Image Understanding, Vol. 77, pp. 211–232, 2000.

[109] Pluim, J., Maintz, J., and Viergever, M., Mutual information matching in multiresolution context, Image and Vision Computing, Vol. 19, No. 1–2, pp. 45–52, 2001.

[110] Powell, M., An efficient method for finding the minimum of a function of several variables without calculating derivatives, The Computer Journal, pp. 155–162, 1964.

[111] Press, W., Teukolsky, S., Vetterling, V., and Flannery, B., Numerical Recipies in C, 2nd edn, Cambridge University Press, 1992.

[112] Reissman, P. J., and Magnin, I. E., The active pyramid : a new tool for modelling 3D deformable object, International Journal Pattern Recognition on Artificial Intelligence, Vol. 11, No. 7, pp. 1129–1139, 1997.

[113] Roche, A., Malandain, G., and Ayache, N., Unifying maximum likelihood approaches in medical image registration, International Journal of Imaging Systems and Technology: Special Issue on 3D Imaging, Vol. 11, No. 1, pp. 71–80, 2000.

[114] Rohr, K., On 3D differential operators for detecting point landmarks, Image and Vision Computing, Vol. 15, No. 3, pp. 219–233, 1997.

[115] Rohr, K., Extraction of 3D anatomical point landmarks based on invariance principles, Pattern Recognition, Vol. 32, pp. 3–15, 1999.

[116] Rohr, K., Stiehl, H., Sprengel, R., Beil, W., Buzug, T., Weese, J., and Kuhn, M., Point-based elastic registration of medical image using approximating thin-plate splines, In: Proc. Visualization in Biomedical Computing, Hohne, H. and Kikinis, R., eds., No. 1131 in Lecture Notes in Computer Science, pp. 297–306, Springer, September 1996, Hamburg.

[117] Rueckert, D., Somoda, I., Hayes, C., Hill, D., Leach, M., and Hawkes, D., Non-girid registration using free-form deformations: application to breast MR images, IEEE Transactions on Medical Imaging, Vol. 18, No. 8, pp. 712–721, 1999.

[118] Sandor, S. and Leahy, R., Surface-based labeling of cortical anatomy using a deformable atlas, IEEE Transactions on Medical Imaging, Vol. 16, No. 1, pp. 41–54, 1997.

[119] Schnabel, J. A., Tanner, C., Castellano-Smith, A. D., Degenhard, A., Leach, M. O., Hose, D. R., Hill, D. L. G, and Hawkes, D. J., Validation of non-rigid image registration using finite element methods: Application to breast MR images, IEEE Transactions on Medical Imaging, Vol. 22, No. 2, pp. 238– 247, 2003.

[120] Schnörr, C., A study of convex variational diffusion approach for image segmentation and feature extraction, Journal of Mathematical Imaging and Vision, Vol. 8, No. 3, pp. 271–292, 1998.

[121] Schormann, T., Henn, S., and Zilles, K., A new approach to fast elastic alignement with application to human brains, In: Proc. Visualization in Biomedical Computing, Hohne, K. H., and Kikinis, R., eds., No. 1131 in Lecture Notes in Computer Science, pp. 337–342, Springer, September 1996.

[122] Schroeter, P., Vesin, J., Langenberger, T., and Meuli, R., Robust parameter estimation on intensity distribution for brain magnetic resonance images, IEEE Transactions on Medical Imaging, Vol. 17, No. 2, pp. 172–186, 1998.

[123] Sederberg, T. and Parry, S., Free-form deformations of solid geometric models, Computer Graphics (SIGGRAPH), Vol. 20, No. 4, pp. 151–160, 1986.

[124] Sethian, J. A., Level Set Methods, Cambridge University Press, 1996.

[125] Song, S. and Leahy, M., Computation of 3D velocity fields from 3D cine CT images of a human heart, IEEE Transactions on Medical Imaging, Vol. 10, No. 3, pp. 295–306, 1991.

[126] Subsol, G., Thirion, J. P., and Ayache, N., A general scheme for automatically building 3D morphometric anatomical atlases: application to a skull atlas, Medical Image Analysis, Vol. 2, No. 1, pp. 37–60, 1998.

[127] Szeliski, R. and Coughlan, J., Hierarchical spline-based image registration, In: Proc. Conference Computer Vision Pattern Recognition, pp. 194–201, Seattle, June 1994.

[128] Szeliski, R. and Lavallée, S., Matching 3D anatomical surfaces with non-rigid deformations using octree-splines, In: SPIE Geometric Methods in Computer Vision, Vol. 2031, pp. 306–315, 1993.

[129] Szeliski, R. and Lavallée, S., Matching 3D anatomical surfaces with non-rigid deformations using octree-splines, Inteternational Journal of Computer Vision, Vol. 18, No. 2, pp. 171–186, 1996.

[130] Talairach, J., Szikla, G., Tournoux, P., Prosalentis, A., and Bornas-Ferrier, M., Atlas d'anatomie stéréotaxique du télencéphale, Masson, Paris, 1967.

[131] Talairach, J. and Tournoux, P., Co-planar Stereotaxic Atlas of the Human Brain, Georg Thieme Verlag, Stuttgart, 1988.

[132] Talairach, J. and Tournoux, P., Referentially Oriented Cerebral MRI Anatomy, Georg Thieme Verlag, New-York, 1993.

[133] Terzopoulos, D., Image analysis using multigrid relaxation methods, IEEE Transactions on Pattern Analysis and Machine Intelligence, Vol. 8, No. 2, pp. 129–139, 1986.

[134] Terzopoulos, D. and Metaxas, D., Dynamic 3D models with local and global deformations: deformable superquadrics, IEEE Transactions on Pattern Analysis and Machine Intelligence, Vol. 13, No. 7, pp. 703–714, 1991.

[135] Thirion, J. P., Extremal points, definition and application to 3D image registration, In: Proc. Conference Computer Vision Pattern Recognition, pp. 587–592, Seattle-Washington, USA, 1994.

[136] Thirion, J. P., Image matching as a diffusion process: an analogy with Maxwell's demons. Medical Image Analysis, Vol. 2, No. 3, pp. 243–260, 1998.

[137] Thirion, J. P., and Gourdon, A., Computing the differential characteristics of isointensity surfaces, Computer Vision and Image Understanding, Vol. 61, No. 2, pp. 190–202, 1995, Available at: http://www.inria.fr/RRRT/RR-1881.html.

[138] Thompson, P. and Toga, A., A surface-based technique for warping three-dimensional images of the brain, IEEE Transactions on Medical Imaging, Vol. 15, No. 4, pp. 402–417, 1996.

[139] Thompson, P., Woods, R., Mega, M., and Toga, A., Mathematical/computational challenges in cretaing deformable and probabilistic atlases of the human brain, Human Brain Mapping, Vol. 9, pp. 81–92, 2000.

[140] Toga, A. and Thompson, P., The role of image registration in brain mapping, Image and Vision Computing, Vol. 19, pp. 3–24, 2001.

[141] Vaillant, M. and Davatzikos, C., Hierarchical matching of cortical features for deformable brain image registration, In: Proc. Information Processing in Medical Imaging, Kuba *et al.*, ed., No. 1613 In Lect. Not. in Comp. Sci., pp. 182–195, Springer, Jun. 1999.

[142] Bemmel, J. H., Van and M. A. Musen, Handbook of Medical Informatics, Springer. Available at http://www.mieur.nl/mihandbook, 1997.

[143] Elsen, P. A. Van den, Pol, E. D., and Viergever, M. A., Medical image matching: a review with classification, IEEE Engineering in Medecine and Biology, Vol. 12, pp. 26–38, 1993.

[144] Vemuri, B., Huang, S., Sahni, S., Leonard, C., Mohr, C., Gilmore, R., and Fitzsimmons, J., An efficient motion estimator with application to medical image registration, Medical Image Analysis, Vol. 2, No. 1, pp. 79–98, 1998.

[145] Viola, P. and Wells, W., Alignment by maximisation of mutual information, In: Proc. International Conference on Computer Vision, pp. 15–23, 1995.

[146] Wang, Y. and Staib, L., Physical model-based non-rigid registration incorporating statistical shape information, Medical Image Analysis, Vol. 4, pp. 7–20, 2000.

[147] West, J., Fitzpatrick, J., Wang, M., Dawant, B., Maurer, C., Kessler, R., and Maciunas, R., Retrospective intermodality registration techniques for images of the head: surface-based versus volume-based, IEEE Trans. Medical Imaging, Vol. 18, No. 2, pp. 144–150, 1999.

[148] Witkin, A. and Welch, W., Fast animatipon and control of non-rigid structures, Computer Graphics (SIGGRAPH), Vol. 24, No. 4, pp. 243–252, 1990.

[149] Zhang, Y., Brady, M., and Smith, S., Segmentation of brain MR images through a hidden markov random field model and the expectation-maximization algorithm, IEEE Transactions on Medical Imaging, Vol. 20, No. 1, pp. 45–57, 2001.

[150] Zhang, Z., Iterative point matching for registration of free-form curves and surfaces, International Journal of Computer Vision, Vol. 13, No. 2, pp. 119–152, 1994.

[151] Zitova, B. and Flusser, J., Image registration methods: a survey, Image and Vision Computing, Vol. 21, pp. 977–1000, 2003.